Local Rossby Wave Packet Amplitude, Phase Speed, and Group Velocity: Seasonal Variability and Their Role in Temperature Extremes

GEORGIOS FRAGKOULIDIS AND VOLKMAR WIRTH

Institute for Atmospheric Physics, Johannes Gutenberg University, Mainz, Germany

(Manuscript received 29 May 2019, in final form 10 July 2020)

ABSTRACT

Transient Rossby wave packets (RWPs) are a prominent feature of the synoptic to planetary upper-tropospheric flow at the midlatitudes. Their demonstrated role in various aspects of weather and climate prompts the investigation of characteristic properties like their amplitude, phase speed, and group velocity. Traditional frameworks for the diagnosis of the two latter have so far remained nonlocal in space or time, thus preventing a detailed view on the spatiotemporal evolution of RWPs. The present work proposes a method for the diagnosis of horizontal Rossby wave phase speed and group velocity locally in space and time. The approach is based on the analytic signal of upper-tropospheric meridional wind velocity and RWP amplitude, respectively. The new diagnostics are first applied to illustrative examples from a barotropic model simulation and the real atmosphere. The main seasonal and interregional variability features of RWP amplitude, phase speed, and group velocity are then explored using ERA5 reanalysis data for the time period 1979–2018. Apparent differences and similarities in these respects between the Northern and Southern Hemispheres are also discussed. Finally, the role of RWP amplitude and phase speed during central European short-lived and persistent temperature extremes is investigated based on changes of their distribution compared to the climatology of the region. The proposed diagnostics offer insight into the spatiotemporal variability of RWP properties and allow the evaluation of their implications at low computational demands.

KEYWORDS: Atmospheric circulation; Rossby waves; Wave properties; Extreme events; Climatology; Fourier analysis

1. Introduction

Rossby waves are a dominant feature of the midlatitude upper-tropospheric circulation at synoptic to planetary scales (Rossby 1940; Haurwitz 1940). Owing their existence to the rotation and the spherical shape of Earth, they take the form of large-scale meanders in the westerly winds (Rhines 2015). On the weather time scale, Rossby wave activity typically varies in longitude and time and tends to organize in the so-called Rossby wave packets (RWPs), rather than circumglobal waves (e.g., Lee and Held 1993; Chang 1993). Although theoretical arguments for the evolution of Rossby waves in idealized setups had already been put forward in the middle of the twentieth century (Dickinson 1978, and references therein), their actual behavior and role in the atmosphere started being investigated in recent decades, facilitated by the increasing data availability and advances in computer performance [see Wirth et al. (2018) for a review of recent developments]. In this regard, recent studies have examined the role of the RWPs evolution in: storm track activity (Nakamura and Wallace 1990; Chang et al. 2002; Hakim 2003; Ahmadi-Givi et al. 2014), the occurrence of weather extremes (Feldstein and Dayan 2008; Wirth and Eichhorn 2014; O'Brien and Reeder 2017; Fragkoulidis et al. 2018), and predictability (Grazzini and Vitart 2015; Quinting and Vitart 2019; Baumgart et al. 2019).

In parallel, ongoing efforts in improving the diagnostic methods of RWPs aim to shed more light on the above considerations. Hovmöller diagrams have been used for the investigation of RWP progression in longitude

Denotes content that is immediately available upon publication as open access.

Supplemental information related to this paper is available at the Journals Online website: https://doi.org/10.1175/JCLI-D-19-0377.s1.

Corresponding author: Georgios Fragkoulidis, gfragkou@uni-mainz.de

DOI: 10.1175/JCLI-D-19-0377.1

© 2020 American Meteorological Society. For information regarding reuse of this content and general copyright information, consult the AMS Copyright Policy (www.ametsoc.org/PUBSReuseLicenses).

Unauthenticated | Downloaded 08/28/22 02:25 AM UTC

and time (Hovmöller 1949; Glatt et al. 2011; Röthlisberger et al. 2019). Computing the envelope of the meridional wind has allowed the development of RWP tracking algorithms and climatological assessments of their preferred regions of formation and decay (Souders et al. 2014b; Glatt and Wirth 2014). Furthermore, the concepts of wave energy flux and wave activity flux have provided insight into the horizontal propagation of linear waves on slowly varying background flows (Plumb 1986; Chang and Orlanski 1994; Takaya and Nakamura 2001; Wolf and Wirth 2017). In addition, the potential vorticity framework has been employed for the analysis of downstream development, baroclinic amplification and other dynamical processes that affect the lifetime of RWPs (Teubler and Riemer 2016).

Two important aspects in the spatiotemporal evolution of RWPs are their phase speed and group velocity. The phase speed reflects the propagation speed of individual troughs and ridges within an RWP and can thus be critical for the persistence of extreme weather (Röthlisberger et al. 2019). When it comes to small wavenumbers (1–3), the zonal component of the phase speed can also affect wave propagation into the stratosphere and the evolution of sudden stratospheric warming events (Domeisen et al. 2018). Group velocity, on the other hand, indicates how fast the wave packet propagates as a whole and reflects the rate at which energy is transferred by the Rossby waves (e.g., Pedlosky 2003; Cai and Huang 2013). Previous modeling and observational studies have investigated variations of the group velocity field within RWPs and how they reflect dynamical processes of their generation and maintenance (Pierrehumbert and Swanson 1995; Esler and Haynes 1999b; Chang 2001b). Especially amid the complexity of the real atmosphere, both the RWP phase speed and group velocity fields are not expected to be homogeneous. Changes in the shape of RWPs during their lifetime owing to, among other factors, the dispersive nature of Rossby waves, downstream development, the interplay with dynamical and thermodynamical processes across scales, and the interaction with other RWPs imply that these fields will generally vary in space and time. Based on that, the not so intuitive concepts of local phase, wavenumber, and angular frequency have to be adopted in order to diagnose and interpret the local phase speed and group velocity of RWPs.

Diagnostic methods regarding these two aspects have so far remained nonlocal in space or time and are thus not suited to follow the evolution of an RWP at high spatial and temporal resolution. For example, Blackmon et al. (1984) proposed a method to calculate phase speed based on lag-correlation maps, which was later also used for the diagnosis of group velocity (Berbery and Vera 1996; Chang and Yu 1999). The resulting fields are local in space, but not local in time; the computation of lag-correlation maps for a given grid point involves the evolution of the meridional wind (or envelope) field over the whole dataset (as in the climatological analyses of the aforementioned studies) or a period of several days (Takaya and Nakamura 2001). In other studies, a Fourier analysis has been used for the diagnosis of phase speed for given wavenumbers (e.g., Randel and Held 1991; Coumou et al. 2014). In this case, the phase speed measure may be instantaneous, but there is no longitudinal information. Obviously, estimates of the zonal phase speed and group velocity can also be extracted from Hovmöller diagrams (Joung and Hitchman 1982; Lee and Held 1993), but they are sensitive to the way the diagram is constructed and lack locality in space and time. It is also worth mentioning, that in the case of linear waves in a slowly varying background flow (WKB approximation), the group velocity is given by the ratio of the wave activity flux to the wave activity density (Chang and Orlanski 1994; Vanneste and Shepherd 1998; Chang 2001b).

In this study, we employ a method that was originally developed by Gabor (1946) for analyzing the instantaneous frequency in time-varying signals. The method involves the *analytic signal*, a complex-valued representation of a real signal that can uniquely define its instantaneous amplitude and phase (Cohen 1995). Computing the analytic signal of the meridional wind along latitude circles allows the identification of the local phase within RWPs, which can then be used to diagnose the zonal component of the local phase speed. In a similar way, we propose an object-based approach for the diagnosis of the zonal and meridional group velocity using the RWP amplitude field. These local diagnostics will allow us to investigate the seasonal patterns and variability of important RWP properties, as well as their role in temperature extremes of a specific region.

This paper is organized as follows. After a brief description of the data used (section 2), we present the methodology for the diagnosis of the local and instantaneous amplitude, phase speed, and group velocity in section 3. Exemplary applications to barotropic model and reanalysis data provide insight into these novel diagnostics. In section 4 we report on the seasonal and interregional variability of the diagnosed variables, while in section 5 we investigate the role of RWP phase speed and amplitude in central European temperature extremes. Finally, our results are summarized in section 6, along with a discussion of their implications and limitations. Computational details and additional analyses that support the interpretation of the presented methods and results are included in the supplemental material (SM).

Unauthenticated | Downloaded 08/28/22 02:25 AM UTC

2. Data

In this study we use ERA5 reanalysis data [Copernicus Climate Change Service (C3S) 2017] for the period from January 1979 to December 2018. In particular, zonal and meridional wind (u and v) at 300 hPa, geopotential height (Z) at 500 hPa, and temperature (T) at 850 hPa have been retrieved at a 6-hourly temporal resolution (daily at 0000, 0600, 1200, and 1800 UTC) on a grid of $2° \times 2°$ horizontal resolution. Furthermore, in section 3 the steps of the presented diagnostic methods are illustrated using 6-hourly meridional wind output from the barotropic model simulation of Ghinassi et al. (2018) at $2° \times 2°$ horizontal resolution.

The retrieved reanalysis fields are preprocessed as follows:

(i) The anomalous components of v, Z, and T, denoted by v', Z', and T', respectively, are computed by removing at each grid point (λ: longitude, ϕ: latitude) and time instance t the corresponding value of a smooth annual cycle:

$$\psi'(\lambda,\phi,t) = \psi(\lambda,\phi,t) - \overline{\psi}(\lambda,\phi,t_d), \qquad (1)$$

where ψ represents the variable (v, Z, or T), $\overline{\psi}$ represents the annual cycle, and t_d denotes a particular time step in the year (e.g., 1200 UTC 15 February). The annual cycle is obtained by first averaging the variable for each t_d over the 40 years available (1979–2018), followed by a Fourier series expansion and restriction to frequencies 0–4 yr^{-1}.

(ii) The meridional wind anomaly, v', is zonally filtered as described in Fragkoulidis et al. (2018). Essentially, from the v' full field spectrum we keep wavelengths of 2000–10 000 km, which roughly correspond to zonal wavenumbers 3–15 at 40°N. Discontinuities in the meridional direction that may arise from this zonal filtering are then minimized by convolving a Hann window (Harris 1978) of 7° length at half maximum in the meridional direction. For consistency, this spatial filtering is also applied to the barotropic model v field.

The ensuing smoothing of the meridional wind field in the last step is weak enough to leave the local RWP characteristics and their transient evolution unaffected, but at the same time strong enough to avoid spurious values from fine-scale features (see section 1 of the SM for an illustration).

3. Diagnosis of local RWP phase speed and group velocity

As mentioned in the introduction, the main goal of this study is to develop a method for the diagnosis of RWP phase speed and group velocity locally in space and time. The rationale, formulations, and illustrative examples of our procedure are presented in this section. Our point of departure is the upper-tropospheric (300 hPa) meridional wind field, where successions of northerlies and southerlies at scales of a few thousand kilometers constitute a clear manifestation of Rossby waves. Therefore, this field is well suited and, indeed, has traditionally been used for the investigation of RWP properties (e.g., Chang 1993). Focusing on an individual latitude circle of meridional wind, the zonal component of the RWP phase speed corresponds to the rate at which a point of constant phase propagates in the zonal direction. Local in time and longitude information of the phase within the RWPs would allow us to compute the local phase speed as the ratio of the local angular frequency to the local angular wavenumber. A similar approach applied to the envelope of the meridional wind would allow the computation of the local group velocity.

Based on this line of thought, determining the local phase is the key step toward our objective. To this end, the analytic signal of the meridional wind and envelope functions along latitude circles is employed. Past studies in the field of signal processing have investigated in detail the advantages and limitations of the analytic signal approach in detecting the instantaneous phase and frequency of time-varying signals (Cohen 1995; Huang et al. 1998, 2009). An implicit requirement for this method to give physically meaningful results in our case is that, ''locally,'' the meridional wind signal needs to have the form of an almost plane wave. More specifically, it is assumed that the wave signal is characterized locally by a clearly discernible dominant wavenumber and angular frequency.[1] These conditions are illustrated and discussed in sections 2 and 4 of the SM. In practice, flow features across scales in the upper troposphere cannot always be attributed to waves of slowly varying properties, which means that these conditions will not be uniformly met. The preprocessing of meridional wind and specific steps in the methodology to be presented in this section aim at minimizing the effect of these limitations (see also discussion in section 6).

a. Analytic signal and local phase

In the following, the meridional wind anomaly along a latitude circle is written as the sequence v'_ℓ, where $\ell = 0, 1, \ldots, L-1$ (L being an even number) denotes

[1] In section 4 of the SM, an example of a wavelet transform along a latitude circle reveals how meridional wind along a latitude circle is generally composed of a spectrum of wavenumbers at each longitude.

Unauthenticated | Downloaded 08/28/22 02:25 AM UTC

the grid point that is located at longitude $\lambda = 2\pi\ell/L$ (with $0 < \lambda \leq 2\pi$). Following Marple (1999), the analytic signal of v'_ℓ is given by

$$A_{v'_\ell} = \frac{1}{L}\sum_{m=0}^{L-1} \tilde{A}_m \, e^{2im\pi\ell/L}, \tag{2}$$

with

$$\tilde{A}_m = \begin{cases} \tilde{v}'_m, & \text{for } m = 0,\ L/2, \\ 2\tilde{v}'_m, & \text{for } 1 \leq m \leq L/2 - 1, \\ 0, & \text{for } L/2 + 1 \leq m \leq L - 1, \end{cases} \tag{3}$$

where m is the spatial frequency (wavenumber) and $\tilde{v}'_m$ is the discrete Fourier transform of v'_ℓ:

$$\tilde{v}'_m = \frac{1}{L}\sum_{\ell=0}^{L-1} v'_\ell \, e^{-2im\pi\ell/L}. \tag{4}$$

Based on the seminal work of Gabor (1946), by suppressing the negative half of the v'_m frequency spectrum (which is redundant for a real signal, since its spectrum is conjugate symmetric: $\tilde{v}'_{+m} = \tilde{v}'^{*}_{-m}$), $A_{v'_\ell}$ becomes a complex function. Its real part, $\mathrm{Re}[A_{v'_\ell}]$, corresponds to v'_ℓ, while its imaginary part, $\mathrm{Im}[A_{v'_\ell}]$, corresponds to the Hilbert transform of v'_ℓ (Gabor 1946; Cohen 1995).[2]

Given the complex representation of $v'_\ell(A_{v'_\ell})$ it is now possible to obtain the local amplitude and phase of wavelike fluctuations in longitude. Namely, when $A_{v'_\ell}$ is expressed in polar form:

$$A_{v'_\ell} = |A_{v'_\ell}| \, e^{i\mathrm{Arg}\{A_{v'_\ell}\}} = E_\ell \, e^{i\Phi_{v'_\ell}}, \tag{5}$$

it can be seen that $E_\ell = |A_{v'_\ell}|$ is the envelope function (local amplitude) and

$$\Phi_{v'_\ell} = \tan^{-1}\left(\frac{\mathrm{Im}[A_{v'_\ell}]}{\mathrm{Re}[A_{v'_\ell}]}\right) \tag{6}$$

is the local phase of v'_ℓ (e.g., Cohen 1995).[3] This formulation for the local phase was recently used for the extraction of the local wavenumber in gravity waves (Schoon and Zülicke 2018). A similar expression for the local RWP phase appeared in the past [Eq. (32) in Hayashi 1982], but to the best of our knowledge it has not been exploited further since then. Several studies have focused on the envelope E as a measure of the local RWP amplitude (e.g., Zimin et al. 2003; Glatt and Wirth 2014; Souders et al. 2014a; Wolf and Wirth 2015; Fragkoulidis et al. 2018). In this study, the local phase Φ constitutes the key element for the diagnosis of Rossby wave phase speed and group velocity locally.

b. Local RWP phase speed

The phase at time t and location x for a plane wave of angular frequency ω and zonal angular wavenumber k that propagates at a certain altitude along a certain latitude is given by

$$\Phi = kx - \omega t + \Phi_0 \,, \tag{7}$$

where $x = a\cos\phi\lambda$ and Φ_0 is a constant offset (a denotes Earth's radius). The units of ω and k are radians per second ($\mathrm{rad\,s^{-1}}$) and radians per meter ($\mathrm{rad\,m^{-1}}$), respectively. Phase speed corresponds to the rate of propagation of a point of constant phase and can be defined as the ratio of angular frequency ω to angular wavenumber k. In the following, phase speed will always refer to a speed relative to the surface of Earth.

A first necessary step is to compute the RWP amplitude E as the modulus of $A_{v'_\ell}$. The resulting field is zonally filtered to only keep wavelengths above 4000 km, in a way similar to v'. This wavelength threshold is consistent with the lower threshold we use for the v' zonal filtering. A hypothetical trough–ridge pattern of 2000-km wavelength would be "enveloped" by a function that has double this wavelength.

The local phase $\Phi_{v'_\ell}$ at all points ℓ of a given latitude circle is then computed through (6). Subsequently, the phase speed c_p at ℓ corresponds to the ratio of $\omega_{v'_\ell}$ to $k_{v'_\ell}$:

$$c_p = \frac{\omega_{v'_\ell}}{k_{v'_\ell}}, \tag{8}$$

$$\text{where} \quad \omega_{v'_\ell} = -\frac{\partial\Phi_{v'_\ell}}{\partial t}, \quad \text{and} \tag{9}$$

$$k_{v'_\ell} = \frac{1}{a\cos\phi}\frac{\partial\Phi_{v'_\ell}}{\partial\lambda}. \tag{10}$$

The derivatives in longitude and time are calculated using centered differences (see also section 3 in the SM) and positive (negative) c_p values correspond to eastward (westward) propagation relative to the ground. The above calculations are repeated for every latitude, so that we get the two-dimensional c_p field. Since individual troughs and ridges within RWPs move predominantly in

[2] Instead of using (2), another way to get the analytic signal is by forming $A_{v'_\ell} = v'_\ell + i\mathscr{H}[v'_\ell]$, where the Hilbert transform $\mathscr{H}$ is computed as $\mathscr{H}[v'_\ell] = \mathscr{F}^{-1}\{-i\mathrm{sgn}(m)\tilde{v}'_m\}$ (e.g., Chaudhury and Unser 2009). Here $\mathscr{F}^{-1}$ denotes the inverse discrete Fourier transform and sgn is the sign function.

[3] The function atan2 (two-argument variant of arctangent) is used to calculate the principal value of the argument ($\mathrm{Arg}\{A_{v'_\ell}\}$), because it accounts for angles in all four quadrants.

Unauthenticated | Downloaded 08/28/22 02:25 AM UTC

the zonal direction, we focus attention on zonal phase speed only.

The result of (8) is physically meaningful to the extent that the $\omega_{v'_\ell}$ and $k_{v'_\ell}$ values are discernible features of the meridional wind signal locally in space and time. Therefore, areas of weak E values associated with the incoherent evolution of small-scale features or the often diffusive edges of RWPs may result in spurious c_p values (e.g., Fig. S8 in the SM). As implied in the introductory paragraphs of this section, the notion of phase propagation is anyway ambiguous in parts of the flow where there is no well-defined wave propagation. To this end, the computation of $\omega_{v'_\ell}$, $k_{v'_\ell}$, and, therefore, c_p is restricted to grid points where the RWP amplitude exceeds a certain threshold E_0. In particular, if δt and $\delta\lambda$ are the time step and longitudinal interval of the data, respectively, c_p at (λ, ϕ, t) is only computed when $E \geq E_0$ at (λ, ϕ, t), $(\lambda, \phi, t + \delta t)$, $(\lambda, \phi, t - \delta t)$, $(\lambda + \delta\lambda, \phi, t)$, and $(\lambda - \delta\lambda, \phi, t)$.

The choice of the E_0 threshold is subjective. It has to be large enough for the aforementioned reasons, but not too large as it will limit our analysis to the very strong RWPs. For the barotropic model illustration in the end of this section, we set E_0 to $3\,\mathrm{m\,s^{-1}}$, as this envelope contour outlines the main body of the two particular RWPs. For all other investigations that are based on reanalysis data, we choose a threshold of $15\,\mathrm{m\,s^{-1}}$. This threshold remains fixed for all seasons. Since one of our main goals is to investigate the seasonal variability of the local RWP properties, we do not want seasonality in the threshold to have an effect. Nevertheless, meaningful variations in E_0 do not lead to qualitative changes in the results of sections 4 and 5 (see also discussion in section 6).

c. Local RWP group velocity

The propagation of the wave packet as a whole is less confined in the zonal direction and can attain discernible meridional components. This calls for a diagnosis of both the zonal and meridional components of the group velocity (vector) field: $\mathbf{c}_g = (c_{gx}, c_{gy})$. The two components can be inferred from the evolution of the envelope field E associated with the RWP that embodies the troughs and ridges. Our proposed method for the local (in space and time) group velocity diagnosis shares the basic principle with the one of the phase speed, using the E function instead of v'. Therefore, group velocity is defined here as the rate at which flow features of enhanced meridional wind amplitude propagate in the zonal and meridional directions. Consequently, this definition connotes an extension of the traditional group velocity concept in Rossby wave theory (section 5 in the SM) to large-amplitude waves. As mentioned in the introduction, the temporal evolution of the envelope field has also been used for the estimation of group velocity characteristic values in the studies of Chang and Yu (1999) and Chang (1999).

As discussed before, certain conditions have to be met in order to get physically meaningful information of the local phase, angular wavenumber, and angular frequency of a wave signal. The main difficulty with group velocity arises from the fact that E is a positive-definite quantity, unlike v and v' that naturally fluctuate between positive and negative values. Simply removing the global zonal mean of E can potentially lead to erroneous phase diagnosis in cases when two RWPs of different amplitude and/or length evolve at the same latitude circle (see Fig. S5 for such an example).

Our way forward is an object-based diagnosis of the local E phase, where each individual RWP is treated separately. Given the E field, the procedure for the diagnosis of local group velocity in the zonal direction c_{gx} at time t_0 along a latitude circle involves the following steps:

(i) Grid points that exceed E_0 are regarded to be part of an RWP. If the length $\mathscr{L}$ of a detected RWP object exceeds $\mathscr{L}_0 = 20°$ in longitude, we compute its "envelope anomaly" signal E'_ℓ. This is done, by subtracting at each grid point ℓ that it spans the mean envelope over these grid points:

$$E'_\ell = E_\ell - \frac{\delta\lambda}{\mathscr{L}} \sum_{\ell=\ell_1}^{\ell_2} E_\ell, \quad \text{for} \quad \ell_1 \leq \ell \leq \ell_2, \quad (11)$$

where ℓ_1 and ℓ_2 are the first and final grid points that the object spans ($\ell_2 - \ell_1 = \mathscr{L}/\delta\lambda$). At these grid points, E'_ℓ now corresponds to a signal that is, ideally, an almost plane wave of wavenumber 1 (i.e., with a local maximum at the middle and a local minimum at the boundary; see also Fig. 1 and Fig. S3 for a visualization).[4] The same is done for all other detected RWPs along this latitude circle. The reason why we restrict to lengths above $\mathscr{L}_0$ is to avoid dealing with flow features that are too small to be regarded RWPs.

(ii) For each detected RWP of length $\mathscr{L}$ we seek the location of the corresponding E_ℓ segments at the preceding and succeeding time steps ($t_0 - \delta t$, $t_0 + \delta t$) that will be used for the angular frequency calculation. These segments need to be of length $\mathscr{L}$

[4] Despite the zonal filtering in E, real-atmosphere RWPs will often exhibit E'_ℓ signals that deviate from this behavior. The method still works when there is an equal number of zero crossings and local extrema, but may fail when, for example, three extrema are found between two zero crossings (e.g., Fig. S8).

Unauthenticated | Downloaded 08/28/22 02:25 AM UTC

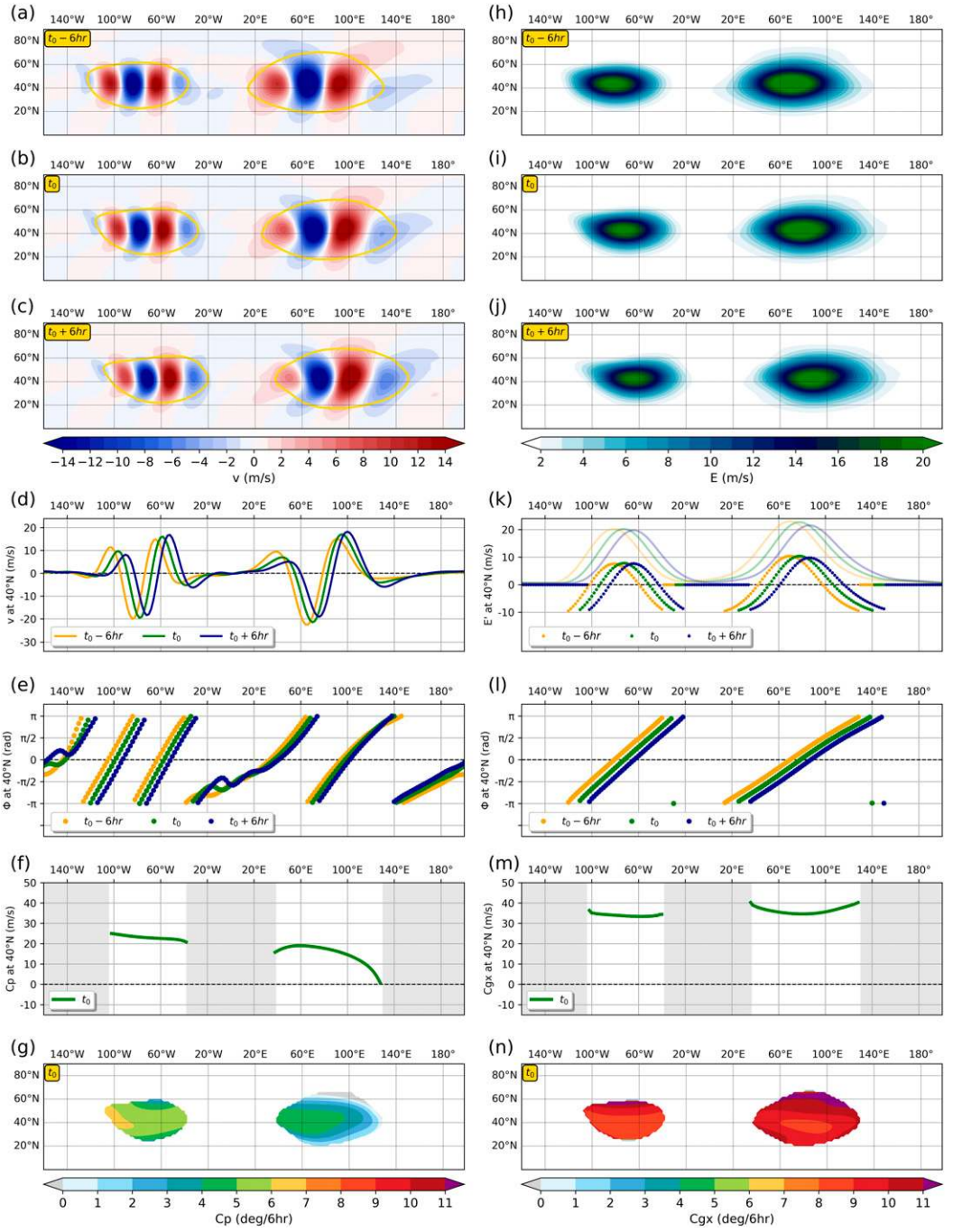

FIG. 1. Illustration of the c_p and c_{gx} diagnosis in the barotropic model simulation: (a)–(c) v at three consecutive 6-hourly time steps (color shading) and isoline of $E_0 = 3\,\mathrm{m\,s^{-1}}$ (yellow contour), (d) v_ℓ evolution at 40°N, (e) Φ_{v_ℓ} evolution at 40°N, (f) c_p at 40°N, (g) map of c_p at t_0, (h)–(j) E at the three consecutive 6-hourly time steps, (k) E_ℓ (solid lines) and E'_ℓ (dotted lines) evolution at 40°N, (l) $\Phi_{E'_\ell}$ evolution at 40°N, (m) c_{gx} at 40°N, and (n) map of c_{gx} at t_0. Orange, green, and blue colors in (d)–(f) and (k)–(m) correspond to the $t_0 - 6\,\mathrm{h}$, t_0, and $t_0 + 6\,\mathrm{h}$, time steps, respectively (as indicated in the legends). Gray shading in (f) and (m) indicates longitudes where c_p and c_{gx} are not defined.

Unauthenticated | Downloaded 08/28/22 02:25 AM UTC

as well and are chosen to span the longitudinal ranges that maximize the sum of E_ℓ, within a search area of $\mathscr{L} + 2\mathscr{L}_0$ degrees longitude. This search area covers the original RWP object (at t_0) plus $\mathscr{L}_0$ degrees to its left and right. The E'_ℓ at this segment is then computed at $t_0 - \delta t$ and $t_0 + \delta t$ by subtracting the respective object zonal mean. The requirement to have equal-length segments of E'_ℓ in the three consecutive instances of the RWP object is discussed in section 3 of the SM. The periodicity of the domain is properly accounted for in these first two steps, so that RWPs around the boundary (prime meridian in this case) are not treated as two distinct objects.

(iii) For each detected RWP object we compute the analytic signal $A_{E'_\ell}$ and local phase $\Phi_{E'_\ell}$ at $t_0 - \delta t$, t, and $t_0 + \delta t$, by applying (2) and (6), respectively, on the corresponding E'_ℓ segment of the three time steps (instead of the v'_ℓ latitude circles). Given the way these E'_ℓ segments are detected, one can assume that they are close to periodic and spurious values in the discrete Fourier transform of (2) are avoided. The aforementioned restriction of the envelope field to wavelengths above 4000 km minimizes the effect of possible wiggles in E'_ℓ that may locally lead to spurious values of c_{gx}.

(iv) The zonal angular frequency $\omega_{E'_\ell}$ and angular wavenumber $k_{E'_\ell}$ are calculated as in (9) and (10), respectively, at longitudes where $\Phi_{E'_\ell}$ is defined for the two points that are involved in the centered differences. That is, $k_{E'_\ell}$ is not computed at the two edges of the detected RWP object and $\omega_{E'_\ell}$ is not computed at longitudes that the RWP object does not occupy at either of the $t_0 - \delta t$ and $t_0 + \delta t$ time steps. The latter implies that the temporal resolution of the dataset has to be high enough, such that it allows enough overlap of the RWP object at consecutive time steps. The 6-h resolution in our case ensures a large overlap for the typical group velocities.

(v) Finally, c_{gx} is computed as the ratio of $\omega_{E'_\ell}$ to $k_{E'_\ell}$ at longitudes where both of them have been computed.

These steps are then repeated for every latitude, so that we get the two-dimensional c_{gx} field. Positive (negative) c_{gx} values correspond to eastward (westward) group propagation relative to the ground.

When it comes to the meridional component of local group velocity c_{gy} the aforementioned steps are applied to the envelope function along meridians E_n in order to account for the evolution of RWPs in latitude. Here, the index n ($n = 0, 1, \ldots, N-1$) corresponds to the latitude ϕ. The procedure is the same as for c_{gx}, except that we seek RWP objects in the meridional direction, the width $\mathcal{N}$ of which exceeds $\mathcal{N}_0 = 10°$ in latitude. The equivalent search area of step (ii) is then equal to $\mathcal{N} + 2\mathcal{N}_0$ degrees latitude (or less in case of an RWP close to the pole). The local phase $\Phi_{E'_\ell}$ is computed for each detected RWP object, based on the envelope anomaly E'_ℓ from the mean along the meridional segment it spans.

The meridional angular frequency $\omega_{E'_n}$ is calculated as in (9) and the meridional angular wavenumber $k_{E'_n}$ is calculated as $a^{-1}\partial\Phi_{E'_n}/\partial\phi$, at latitudes where $\Phi_{E'_n}$ is defined for the two points that are involved in the centered differences. At latitudes where both are computed, c_{gy} is given by the ratio of $\omega_{E'_n}$ to $k_{E'_n}$. Positive (negative) c_{gy} values correspond to northward (southward) group propagation relative to the ground. Finally, the calculations are repeated for every longitude, so that we get the two-dimensional c_{gy} field.

Given that the evolution of RWPs is not always coherent, diagnosing their properties locally and instantaneously can at times lead to unphysical values. Even when restricting to grid points exceeding E_0, a noisy evolution of the v' and E fields can cause a jumpy behavior of $\Phi_{v'}$, $\Phi_{E'_\ell}$, and $\Phi_{E'_n}$ in space and/or time. Rare cases where c_p, c_{gx}, or c_{gy} unphysically exceed $|100|$ m s^{-1} are masked (this masking has no noticeable effect in any of the results shown here).

d. Exemplary cases

The aforementioned methods for the diagnosis of the c_p and $\mathbf{c}_g$ fields are first illustrated in the framework of a barotropic model simulation (Figs. 1 and 2), and then applied to a real case using reanalysis data (Fig. 3). The barotropic model simulation involves an idealized setup with two RWPs of different carrier wavenumbers initialized upon a zonal background flow (more details in Ghinassi et al. 2018). The evolution of meridional wind (Figs. 1a–c) and the corresponding envelope (Figs. 1h–j) fields in a 12-h segment of the idealized simulation depict the downstream propagation of the two wave packets.

In the left column of Fig. 1 we present the aforementioned steps for the diagnosis of the two-dimensional c_p field corresponding to the central time step t_0. Figures 1d and 1e show v_ℓ and the corresponding Φ_{v_ℓ}—as derived from (6)—along 40°N at the three consecutive 6-hourly steps. The phase function is "wrapped" since the atan2 function gives values that are constrained to the $(-\pi, \pi]$ interval (6). Its value is positive (negative) when $\mathrm{Im}[A_{v_\ell}]$ is positive (negative), which is the case in the areas of ridges (troughs) (Fig. S4). Due to this wrapping, caution is needed when computing the derivatives in longitude (angular wavenumber) and time (angular frequency). Our procedure in dealing with this issue is given in section 3 of the SM. Based on (8), the c_p values that correspond to the

Unauthenticated | Downloaded 08/28/22 02:25 AM UTC

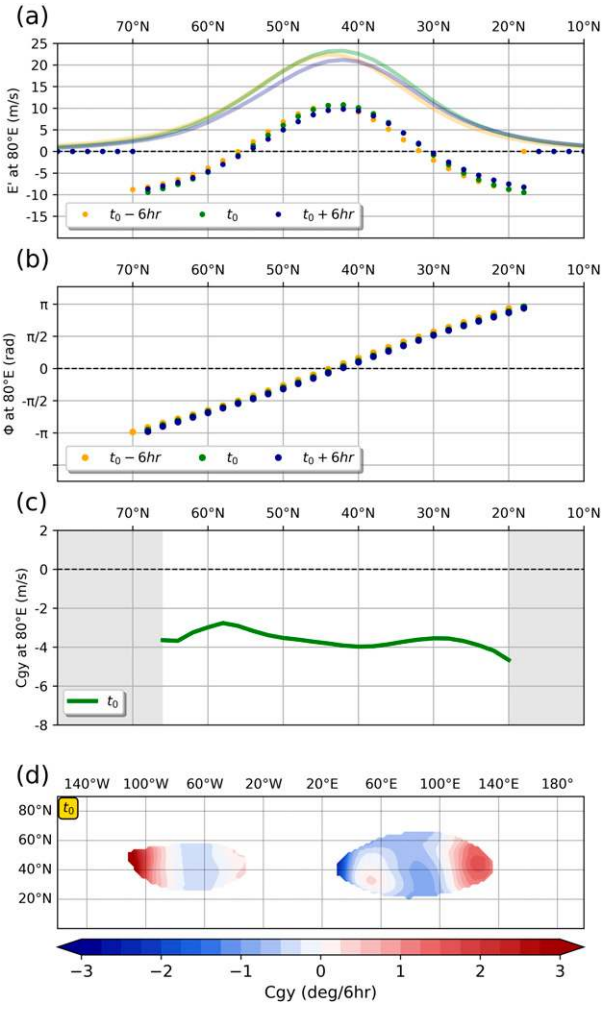

FIG. 2. Illustration of the c_{gy} diagnosis in the barotropic model simulation. (a) E_n (solid lines) and E'_n (dotted lines) at 80°E for the three consecutive 6-hourly time steps, (b) $\Phi_{E'_n}$ evolution at 80°E, (c) c_{gy} at 80°E, and (d) map of c_{gy} at t_0. Orange, green, and blue colors in (a)–(c) correspond to the $t_0 - 6$ h, t_0, and $t_0 + 6$ h time steps, respectively (as indicated in the legends). Gray shading in (c) indicates longitudes where c_{gy} is not defined.

central time step are given in Fig. 1f. Grid points where E is lower than 3 m s^{-1} in any of the neighboring in time or longitude grid points are masked and depicted by gray shading. Repeating the procedure for all latitudes leads to the two-dimensional c_p field (Fig. 1g).

Similarly, in the right column of Fig. 1 we present the steps for the diagnosis of the two-dimensional c_{gx} field corresponding to the central time step t_0. Figure 1k shows in green the E_ℓ and E'_ℓ signals of the two detected RWP objects at time t_0 and latitude 40°N. Orange and blue lines denote the corresponding equal-length RWP objects at $t_0 - \delta t$ and $t_0 + \delta t$, respectively, detected as described in step (ii) of the previous subsection. Figure 1l shows the local phase $\Phi_{E'_\ell}$ of the two RWP objects at the three consecutive time steps. The solitary points close to 20°W and 140°E result from phase wrapping. Figure 1m shows c_{gx} computed along 40°N at longitudes where $\omega_{E'_\ell}$ and $k_{E'_\ell}$ are defined, while Fig. 1n shows the two-dimensional c_{gx} field.

Figure 2 presents the steps for the c_{gy} diagnosis in the same time step of the model simulation. The evolution of E_n, E'_n and $\Phi_{E'_n}$ for the detected RWP object along 80°E is shown in Figs. 2a and 2b. Figure 2c shows c_{gy} computed along 80°E at latitudes where $\omega_{E'_n}$ and $k_{E'_n}$ are defined, while the resulting two-dimensional c_{gy} field is shown in Fig. 2d.

Just for the purposes of presenting the diagnostics, the values of c_p, c_{gx}, and c_{gy} are given in degrees longitude/latitude per 6 h, so that their validity can be visually verified in Figs. 1a–c and 1h–j. The fields are smooth but not entirely homogeneous within the two wave packets, reflecting that—even in this idealized scenario—the shape of the RWPs is not exactly preserved during this 12-h segment. The zonal group velocity exceeds the phase speed everywhere ($c_{gx} > c_p$), indicating the downstream development tendency of Rossby waves. This behavior reflects the fact that the velocity with which energy is transported downstream is larger than the velocity of the individual troughs and ridges (Simmons and Hoskins 1979; Orlanski and Chang 1993; Chang 1993). Furthermore, differences are apparent between the two wave packets, which have similar amplitude but distinct carrier wavenumber. The higher-wavenumber RWP in the Western Hemisphere is associated with generally larger phase speed and lower group velocity than the lower-wavenumber RWP farther downstream. Such behavior can also be anticipated from the theory of free Rossby waves in an inviscid barotropic fluid (e.g., Vallis 2017) (section 5 in the SM).

Figure 3 provides another example of the diagnostics, now in the real-atmosphere evolution of the upper-tropospheric meridional wind during 23 August 2016. Two main areas of enhanced waviness are found over the North Pacific and North Atlantic (Figs. 3a–c and 3e–g). The E_0 threshold of 15 m s^{-1} that is used in this case results in the two RWPs to appear connected or under the process of merging over North America, a situation that illustrates the challenge in selecting the identification threshold for RWP tracking [see Wolf and Wirth (2017) for an extensive discussion of the issue].

The resulting c_p values of the ridge over western Europe and the upstream trough centered at ~20°W amount to 1–4 m s^{-1}, which indicates a quasi-stationary wave (Fig. 3d). As will be shown in the climatological analysis of section 4, this is an unseasonably low phase speed and plausibly critical for the emergence of a late-summer heat wave in western Europe (Zschenderlein et al. 2018). When it comes

Unauthenticated | Downloaded 08/28/22 02:25 AM UTC

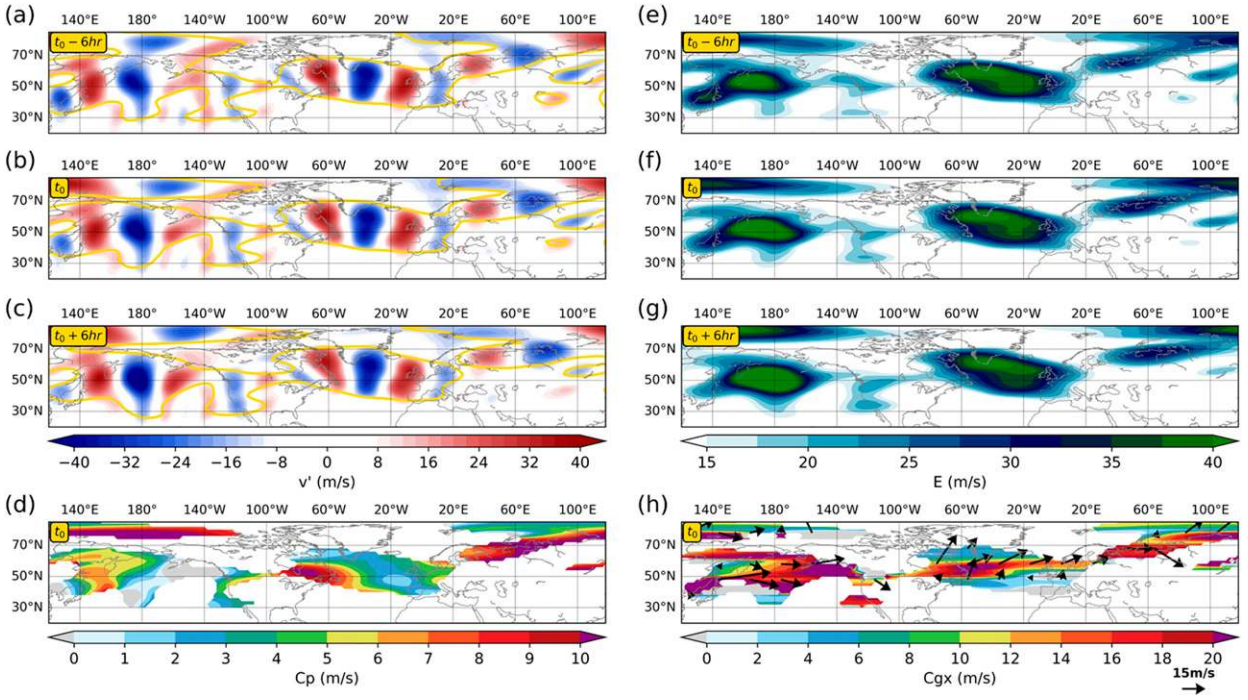

FIG. 3. Illustration of the c_p and $\mathbf{c}_g$ diagnosis at t_0, 1200 UTC 23 Aug 2016: (a)–(c) v' at three consecutive 6-hourly time steps (color shading) and isoline of $E_0 = 15\,\mathrm{m\,s^{-1}}$ (yellow contour), (d) map of c_p at t_0, (e)–(g) E at the three consecutive 6-hourly time steps, and (h) c_{gx} (color shading) and arrows of $\mathbf{c}_g$ (scale is at the lower right) at t_0.

to group velocity, the c_{gx} field is generally noisier than c_p, reflecting the often incoherent and highly transient evolution of RWPs (Fig. 3h). The vector field of $\mathbf{c}_g$ is overlaid in Fig. 3h, hence putting c_{gy} into consideration as well. Based on that, the North Pacific RWP moves predominantly in the zonal direction with an equatorward component at its southernmost parts. The North Atlantic RWP on the other hand, propagates more slowly in the zonal direction with an overall northeastward orientation. It is worth mentioning that there is a small change to the c_{gx} and c_{gy} fields locally, if the E_0 threshold is increased to the point where the two RWPs appear to split (see also discussion in section 6).

As mentioned in the introduction and illustrated in Fig. 3, local and transient features in the upper-tropospheric flow can result in nonuniform c_p and $\mathbf{c}_g$ fields. To a first order, a portion of the spatiotemporal variability can be attributed to varying behavior in different parts of individual RWPs. As an example, the c_p field within the North Atlantic RWP has a pronounced maximum at its trailing edge and a minimum close to its center at around 20°W. Regarding the c_{gx} field of this RWP, there is pronounced variability in latitude, with a maximum between 50° and 60°N and minima at its northern and southern parts. Smaller-scale features in these fields need to be interpreted with caution. The negative c_p values over the Gulf of Alaska, for example, are associated with a band of weak southerlies that are seemingly caught up by the leading edge of an evolving RWP upstream (Figs. 3a–d). For applications where RWPs need to be characterized by single values of phase speed and group velocity, one may compute the areal average of the c_p and $\mathbf{c}_g$ fields over a specified RWP object.

4. Seasonal climatologies

The climatological patterns of the presented local RWP diagnostics are now investigated based on 40 years (1979–2018) of reanalysis data. In particular, maps of the median E, c_p, c_{gx}, and c_{gy} at 300 hPa are presented for each season of the Northern and Southern Hemispheres, followed by a brief discussion in their most distinct features of seasonal and interregional variability. The median is used here as measure of central tendency in the climatological distribution of RWP properties at each grid point since it is less affected by outliers than the mean. Time steps when c_p, c_{gx}, and c_{gy} are not defined (see section 3) are not taken into account for the median calculation. In the case of the RWP amplitude climatologies, the values correspond to the median over time steps when $E \geq 15\,\mathrm{m\,s^{-1}}$ in order to make it consistent with the climatologies of the other fields. The

Unauthenticated | Downloaded 08/28/22 02:25 AM UTC

sample sizes for these conditional climatologies can be inferred from the RWP frequency maps in Fig. S11 of the SM. In addition, Figs. S9 and S10 provide seasonal medians of u and v at 300 hPa to complement the RWP climatologies shown here. At the end of the section, related climatologies derived from the lag-correlation method of Chang and Yu (1999) and the wave activity flux of Plumb (1986) are discussed.

a. Northern Hemisphere

The two first panel rows in Figs. 4a–h quantify the seasonal variability of RWP amplitude E and phase speed c_p, respectively. For most regions in the extratropics a strong seasonality is apparent, associated with the maximization of wave activity during winter and its minimization during summer (see also Souders et al. 2014b), as well as changes in strength and location of the jet streams (Fig. S9). The bands of elevated E and c_p values over the two ocean basins signify the areas where RWPs tend to attain large amplitudes and phase speeds, respectively. The c_p values over the North Pacific and North Atlantic peak during winter at ~11 and ~10 m s^{-1}, respectively. Compared to winter, summer over the North Atlantic is characterized by a decrease of ~4 m s^{-1} in c_p magnitude and a poleward migration of ~10° in the band of maximum values. The transition from winter to summer and vice versa for c_p values is more gradual in the North Atlantic, than in the North Pacific; the latter shows a weak decrease from DJF to MAM, a strong decrease from MAM to JJA and then a gradual increase from JJA to DJF through SON. Throughout the year, over the North Pacific, maximum values of RWP phase speed are found to the west of the date line, while RWP amplitudes maximize to the east of it (roughly 60° longitude downstream). Similarly, over the North Atlantic, c_p maximizes at the narrow band of the jet entrance (Fig. S9), while E maxima extend over a large area of the North Atlantic with increased values maintained all the way to northern Europe (with an apparent poleward orientation during DJF). These results reflect the fact that low-amplitude waves grow in the areas of high baroclinicity (western ocean boundaries) and reach their (amplified) mature stage over the jet exit regions, where the phase speed of their embedded troughs and ridges decreases.

The two bottom rows (Figs. 4i–p) show c_{gx} and c_{gy}. Again, there is a distinct seasonality with values of group velocity maximizing during winter. It is apparent that c_{gx} exceeds c_p by up to 3 times in all seasons (see also Fig. S12). This climatological tendency for downstream development is more pronounced in some regions (e.g., in the subtropical jet) than in others (e.g., the jet exit and cyclolysis region over Europe and the Norwegian Sea). Furthermore, by comparing the c_{gx} maps (Figs. 4i–l) to the respective ones of c_{gy} (Figs. 4m–p), it is apparent that RWP propagation is almost everywhere predominantly zonal ($c_{gx} > |c_{gy}|$).

In most regions, the spatial pattern and seasonal variability of c_{gx} follows closely the ones of zonal wind velocity (Fig. S9). Focusing on the winter season, a distinct band of high c_{gx} values appears in the subtropical jet at a purely zonal orientation (at ~30°N) from northwestern Africa to the North Pacific. Upon it, low-amplitude RWPs (Fig. 4a) propagate eastward at high zonal group velocities (~14–20 m s^{-1}; Fig. 4i) and near-zero meridional "leakage" as indicated by the low meridional group velocity values around it (Fig. 4m). Narrow and elongated as it is, the subtropical jet constitutes an efficient waveguide (e.g., Hoskins and Ambrizzi 1993); a "highway" for transient RWPs that extends over a longitudinal sector of almost 180°. These RWPs can conceivably be excited when breaking waves over Europe (e.g., in the form of PV streamers; Wernli and Sprenger 2007) reach far south to the Mediterranean region and perturb the subtropical jet (Martius et al. 2010). Such a "bridge" between the eddy-driven and the subtropical jet can also be inferred from the enhanced equatorward propagation, in the sense of c_{gy}, over Europe (Fig. 4m). Furthermore, it is upon the subtropical jet where low-frequency teleconnections between distant regions are realized (Branstator 2002). Although less compact, a band of increased c_{gx} values on this waveguide is also observed in the other seasons (Figs. 4j–l).

During all seasons but summer, a secondary branch of relatively high c_{gx} values is evident to the north of the main waveguide (at ~50°N) between 60° and 120°E (see also Chang 2005). This branch follows a more northerly track over Siberia, presumably hosting RWPs that after exiting the poleward oriented North Atlantic jet, reach deep into northern Asia (Fig. 4 and Figs. S9a–d). The study of Chang and Yu (1999) verifies the existence of this secondary Siberian waveguide, with disturbances that originate in Scandinavia and reach the North Pacific after 4 days.

Salient features in the seasonal patterns of c_{gy} do arise and are in good agreement with the ones in the lag-correlation analysis of Chang (1999). Focusing first on winter, positive values of c_{gy} are found to the north and negative values to the south of the North Pacific and North Atlantic jets (Fig. 4m), indicating RWPs that radiate away from the jets toward subpolar and subtropical regions, respectively (Held and Hoskins 1985). Since meridional wave activity divergence and the ensuing zonal momentum convergence lead to eastward jet acceleration (e.g., Vallis 2017), the notion of eddy-driven jets is to some extent reflected in the climatological

Unauthenticated | Downloaded 08/28/22 02:25 AM UTC

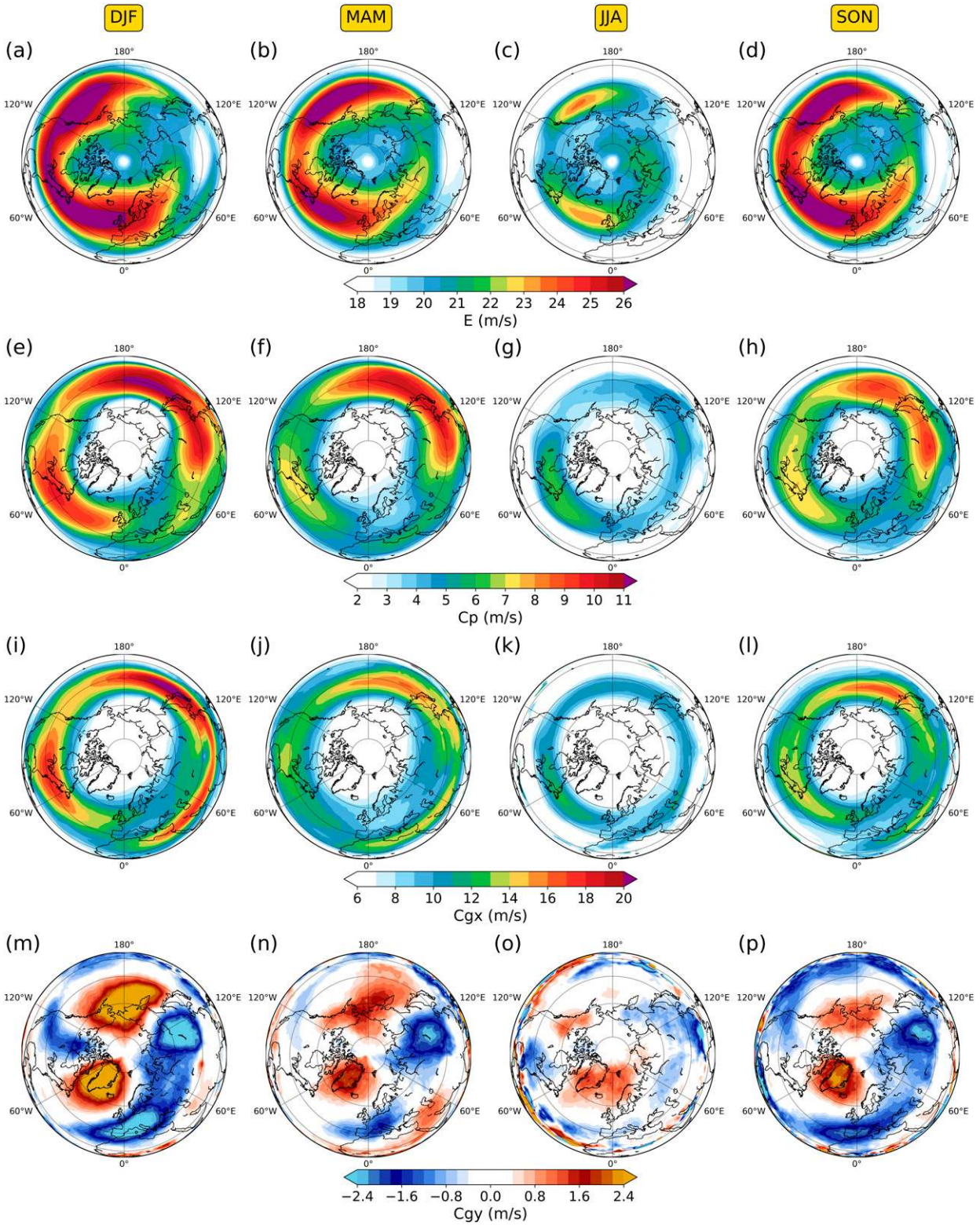

FIG. 4. Northern Hemisphere climatology of RWP properties. Seasonal median of (a)–(d) E, (e)–(h) c_p, (i)–(l) c_{gx}, and (m)–(p) c_{gy} at 300 hPa in the 1979–2018 period. Each column of panels corresponds to the season indicated by the yellow label at the top.

Unauthenticated | Downloaded 08/28/22 02:25 AM UTC

patterns of c_{gy}. From the viewpoint of baroclinic wave life cycles, poleward and equatorward propagation away from the jet latitude is often followed by cyclonic and anticyclonic wave breaking, respectively (Thorncroft et al. 1993; Esler and Haynes 1999a). Past studies in this regard have inferred the meridional propagation of RWPs from the meridional component of wave activity flux (e.g., Esler and Haynes 1999a), the DJF climatological pattern of which (Fig. 6 in Gabriel and Peters 2008) closely resembles the one of c_{gy} in Fig. 4m.

Regarding the other seasons, the c_{gy} patterns do not vary considerably, but the magnitudes do. Minimum values are found in summer, while asymmetries are evident between spring and autumn, with more pronounced negative c_{gy} values to the south of the jets in the latter. A robust feature throughout the year is the equatorward propagation over southeastern Russia and Mongolia (even when the stationary northerly flow over the region—shown in Fig. S10—is removed) (Hsu 1987; White et al. 2017). This feature is associated with the aforementioned secondary c_{gx} branch over Siberia (Joung and Hitchman 1982; Chang and Yu 1999) and, as proposed by previous studies, constitutes an upstream source for cyclone development and Rossby wave initiation over the North Pacific (Hakim 2003; Chang 2005; Röthlisberger et al. 2018).

Worth noting in this analysis is the seasonality of the northwest Pacific, which is characterized during winter by low-level baroclinicity (not shown), strong upper-level zonal winds (Fig. S9), and relatively low E values (Fig. 4) compared to autumn and spring. This feature has been investigated in the past in the context of the Pacific midwinter suppression of eddy activity (Nakamura 1992; Schemm and Schneider 2018), a relevant factor of which is the enhanced RWP group velocity during this period of the year (Chang 2001a). From the seasonal perspective presented here, it is shown in Fig. 4 that there are strong transitions in the c_{gx} and c_{gy} fields from autumn to winter and from winter to spring. The narrow band of enhanced c_{gx} as well as the elevated $|c_{gy}|$ values to the north and south of the jet during winter imply that RWPs have short residence times over the northwestern Pacific. This suggests that developing RWPs exit rapidly this strong part of the jet and only increase in amplitude (and wavenumber; Fig. S15) farther downstream, over the northeastern Pacific (Fig. 4a).

b. Southern Hemisphere

We next focus on the Southern Hemisphere (Fig. 5), where the spatial patterns in E, c_p, c_{gx}, and c_{gy} are characterized by weaker seasonality and exhibit a lesser degree of zonal asymmetry compared to the Northern Hemisphere. In the following, we discuss some of the main aspects in the seasonal variability of the individual fields.

Large E values in summer (DJF) are restricted to a narrow zonal band between 40° and 60°S (locally exceeding 26 m s^{-1}) associated with the midlatitude jet. This band widens in the other seasons, especially over the South Pacific, and the highest amplitudes in many areas are found in autumn. The apparent zonal asymmetry in E and other properties of the circulation is associated with asymmetries in the low-level baroclinicity and tropical SST fields, as well as the tendency for cyclogenesis downstream of the more elevated landmasses (Nakamura and Shimpo 2004; Inatsu and Hoskins 2004).

Although c_p maximizes during winter and spring, in contrast to the Northern Hemisphere, the highest c_{gx} values occur in the fairly zonal and meridionally confined summer midlatitude jet. Generally higher values of u (Fig. S9), c_p, and c_{gx} are found over the South Atlantic and southern Indian midlatitude jets compared to the South Pacific (Souders et al. 2014b). The high values over this sector are associated with enhanced storm track activity and intense SST gradients (Nakamura and Shimpo 2004; Inatsu and Hoskins 2004). The slow phase speed over the South Pacific is also associated with the frequently observed quasi-stationary cyclones over the Ross, Amundsen, and Bellingshausen Seas, an important factor for the more frequent occurrence of cold air outbreaks in that sector of the Southern Hemisphere (Papritz et al. 2015).

A prominent feature of all seasons except summer is the subtropical jet, that gives rise to a double jet circulation between 60°E and 120°W (Fig. S9) (e.g., Nakamura and Shimpo 2004). In its strongest phase during winter (tied to a strengthened Hadley cell), it is characterized by elevated values of c_{gx} over the southern Indian Ocean, Australia, and the southwestern Pacific (15–18 m s^{-1}) and relatively enhanced values of E over the entire South Pacific (22–25 m s^{-1}). Its emergence coincides with a weakening in c_{gx} values over the midlatitude jet. Finally, poleward (equatorward) c_{gy} values to the south (north) of the midlatitude jet are evident.

c. Comparison to the lag-correlation and wave activity methods

As briefly mentioned in the introduction of the paper, the lag-correlation method of Blackmon et al. (1984) has also been used in the past to compute climatologies of the local phase speed and group velocity in the upper-tropospheric flow (Berbery and Vera 1996; Chang and Yu 1999; Chang 1999). Reproducing such an analysis for the Northern Hemisphere winter season shows good agreement with the spatial patterns of Fig. 4 (see section 6 in the SM). Quantitatively, our c_p values are

Unauthenticated | Downloaded 08/28/22 02:25 AM UTC

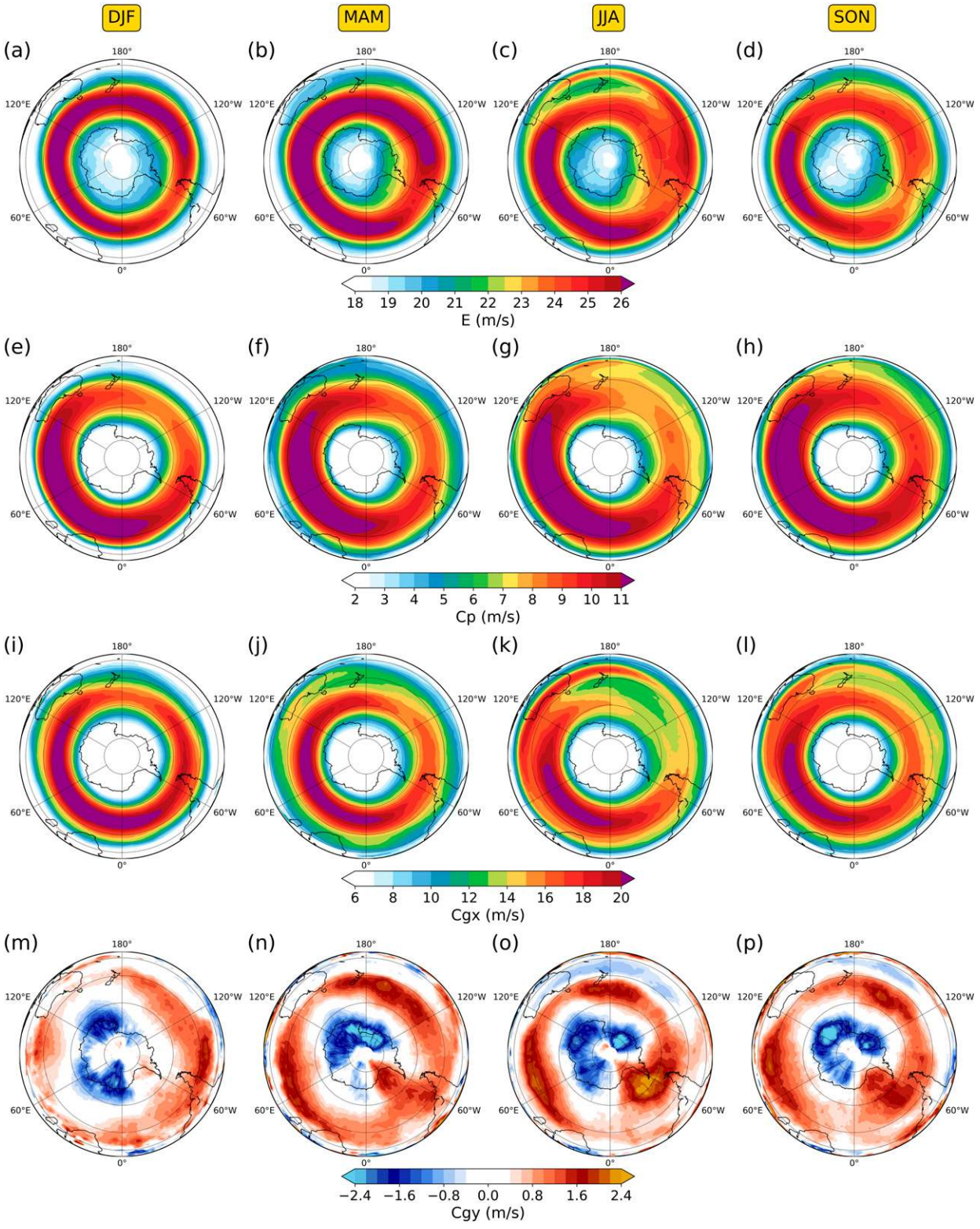

FIG. 5. As in Fig. 4, but for the Southern Hemisphere.

Unauthenticated | Downloaded 08/28/22 02:25 AM UTC

found to be lower by up to 10% in many parts of the globe (Fig. S17). Regarding c_{gy}, there is no apparent difference between the two methods, but in terms of c_{gx}, our values are again found to be lower by 10%–20% (Fig. 6 in Chang and Yu 1999). In absolute terms, these differences are more prominent at the jet cores. An important distinction between the two methods is that our climatological distribution at a given grid point only contains time steps when c_p and c_g are diagnosed, which roughly occurs when $E \geq 15\,\mathrm{m\,s^{-1}}$ (see sections 3b and 3c). Weak perturbations in the more zonal flow regimes that are excluded in our case are expected to propagate downstream at a higher rate, thereby contributing to the aforementioned discrepancies. Indeed, lowering the E_0 threshold of our diagnostic to $10\,\mathrm{m\,s^{-1}}$ leads to higher c_p and c_{gx} values in the storm track regions by about 0.25 and $1\,\mathrm{m\,s^{-1}}$, respectively (see also discussion in section 6). On a more theoretical note, the phase speed of weakly nonlinear waves is predicted to increase with decreasing amplitude (Esler 2004).

Our group velocity climatology as well as the one obtained from the lag-correlation method correspond to the characteristic evolution of the envelope of meridional wind. Such a climatology can also be obtained by taking a different approach that involves the concept of wave activity. In particular, for linear waves in the WKB limit, c_g is given by the ratio of wave activity flux to wave activity density (e.g., Chang 2001b). To this end, Northern Hemisphere winter climatologies of the 300-hPa wave activity flux $\mathbf{M}_T$ and density M based on the formulation of Plumb (1986) for transient eddies are presented here for reference. The involved formulation and results for eddies of various frequencies are included in section 7 of the SM (Fig. S19). In accordance with the results of Plumb (1986), the radiative component of $\mathbf{M}_T$ in the upper troposphere is found to be small compared to the advective one. Consequently, the resulting fields of zonal and meridional group velocity are very close to the DJF mean wind field (Figs. S9a and S10a)—as was also hypothesized in Chang and Yu (1999)—and their magnitudes are substantially higher than the climatologies in Figs. 4i and 4m or the ones of the lag-correlation method. As an example, the values in the North Pacific and North Atlantic storm track entrance regions are ~2.2 times the values of our method. In the storm track exit regions the discrepancy is reduced substantially to a ratio of ~1.7 for the North Pacific and ~1.4 for the North Atlantic.

The aforementioned discrepancy is attributed to differences in the assumptions and limitations between the two methods. Our method is based on the evolution of the meridional wind envelope field and determines the characteristic group velocity of RWPs above a certain amplitude ($15\,\mathrm{m\,s^{-1}}$) that locally resemble almost plane waves. In contrast, the wave activity method is based on linear wave theory, considers the entire time series, and applies to small-amplitude quasigeostrophic waves on a slowly varying background flow (WKB approximation). Although the latter assumptions may be applicable in idealized models of the upper-tropospheric circulation, RWPs in the real atmosphere can deviate significantly from linearity and the WKB limit. Moreover, the propagation of RWPs is expected to be significantly influenced by smaller-scale processes within synoptic eddies and the weaker jet speeds below the level of 300 hPa (see also Chang and Yu 1999). It can therefore be argued that the group velocity climatologies of Figs. 4i and 4m and the lag-correlation method are more direct measures of the observed RWPs than the one based on the wave activity flux.

5. Role of RWP amplitude and phase speed in temperature extremes

In this section, we investigate the role of RWP amplitude E and phase speed c_p in the occurrence and duration of central European hot and cold extremes. To do so, we construct time series of the area-averaged T', E, and c_p fields and examine their climatological covariability for hot/cold persistent and short-lived extremes. The hypothesis is that temperature extremes preferentially occur when an enhanced RWP amplitude characterizes the upper-tropospheric flow (e.g., Fragkoulidis et al. 2018), while their duration is largely influenced by the RWP phase speed.

First, we calculate the daily mean fields of temperature anomaly at 850 hPa, T', E, and c_p for the whole period between January 1979 and December 2018. In the case of c_p, the mean takes into account only time instances when c_p is defined (section 3). If this condition is not met by any of the four time steps during a day, then the daily mean c_p value remains undefined (a "nan" value is given at these grid points). The daily mean T' is then averaged over the 8° × 8° (46°–54°N, 6°–14°E) area (solid rectangle in Fig. 6) with a weighting by the cosine of latitude. The E and c_p daily means are instead averaged over the larger 24° × 24° (38°–62°N, 2°W–22°E) area (dashed rectangle in Fig. 6) in order to capture the synoptic situation around the affected region. The rationale behind this choice is that the temperature over an area is not only affected by the in situ flow. For E and c_p, the area average only accounts for grid points where c_p is defined.

For the purpose of more robust statistics we do not split the analysis in seasons, maintaining nevertheless information about the annual cycle (see below). Therefore, given the complete time series of the area-averaged T' at 850 hPa, cold and hot extremes are detected as follows:

Unauthenticated | Downloaded 08/28/22 02:25 AM UTC

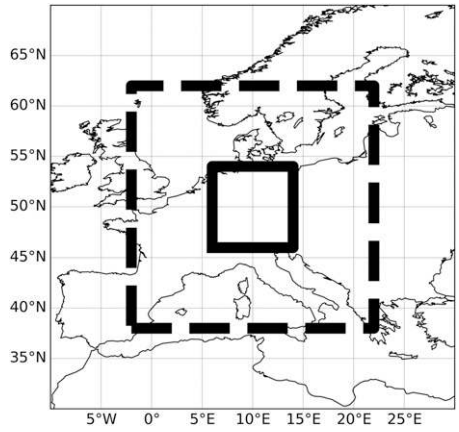

FIG. 6. The two rectangles depict the areas used in averaging E and c_p at 300 hPa (dashed rectangle; 38°–62°N, 2°W–22°E) and T' at 850 hPa (solid rectangle; 46°–54°N, 6°–14°E).

(i) First, the days when the area-averaged T' exceeds the 90th percentile of their respective season constitute hot days, whereas the days when it is smaller than the 10th percentile of their respective season constitute cold days. This selection ensures that each season is equally represented in the analysis. In the following, hot and cold days are jointly referred to as extreme temperature days.

(ii) To examine the covariability of the area-averaged T', E, and c_p time series, we only keep days when the daily mean c_p is defined in at least 10% of the area (17 out of 169 grid points) so that we avoid cases where the area-averaged E and c_p account for just the edge of an RWP (which may not be representative of the synoptic situation; see section 3). This results in discarding 556 out of the total 14 610 days, 19 (15) of which were hot (cold); this corresponds to around 1% of all extreme temperature days.

(iii) Episodes of 1 or 2 extreme temperature days are regarded as *short-lived* extremes, while episodes of 4 or more sequential extreme temperature days are regarded as *persistent* extremes. We leave out episodes that lasted exactly 3 days in order to have a clearer separation and similar distribution sizes of short-lived and persistent extremes (Fig. 7).

Table S1 in the SM shows the resulting statistics for the temperature extremes of each season.

To examine E and c_p in a pool of extreme temperature days from all seasons, the area-averaged E and c_p distributions of each season are normalized by subtracting from each value the seasonal mean and dividing it by the seasonal standard deviation σ. This way each E and c_p value now corresponds to an anomaly with units of standard deviations from its respective seasonal mean.

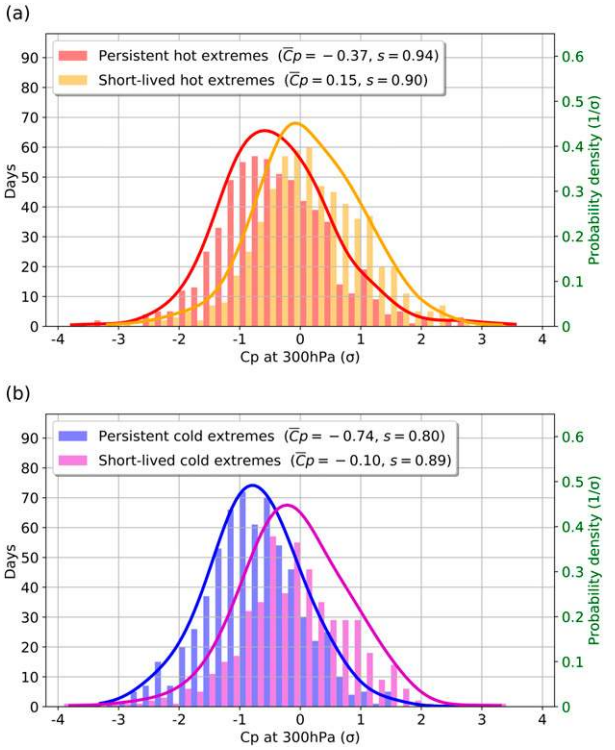

FIG. 7. (a) Histogram (left axis) and the corresponding KDE (right axis) of the normalized area-averaged daily mean c_p at 300 hPa during days of hot extremes over central Europe. Red (orange) colors correspond to persistent (short-lived) hot extremes. Each bin accounts for 0.2σ. (b) As in (a), but for persistent (blue) and short-lived (purple) cold extremes. Shown in the legend is the mean $\overline{c}_p$ and standard deviation s of c_p for each type of extreme. The KDE bandwidth parameter for persistent (short-lived) hot extremes is 0.31 (0.30) and for persistent (short-lived) cold extremes it is 0.34 (0.36).

Figure 7 shows histograms of c_p during hot (Fig. 7a) and cold (Fig. 7b) short-lived and persistent extremes. The mean $\overline{c}_p$ and standard deviation s of the four distributions are shown in the legends of the two panels. Evidently, in persistent hot and cold extremes there is a substantial shift of 0.52 and 0.64 standard deviations, respectively, toward lower c_p values compared to the short-lived ones. Using a Welch's t test for the null hypothesis that the two independent samples have equal means (Ruxton 2006), it is found that the t statistic is 10 and 12.7 for hot and cold extremes, respectively (unequal variances are assumed for the compared samples). The probability to get such values by chance (p value) is well below 0.01, so in both cases the shift toward lower c_p values during persistent extremes is statistically significant at the 1% level. The shift becomes more clear when looking at the corresponding kernel density estimation (KDE) of the distributions (curved lines in Figs. 7a and 7b). This is calculated based on

Unauthenticated | Downloaded 08/28/22 02:25 AM UTC

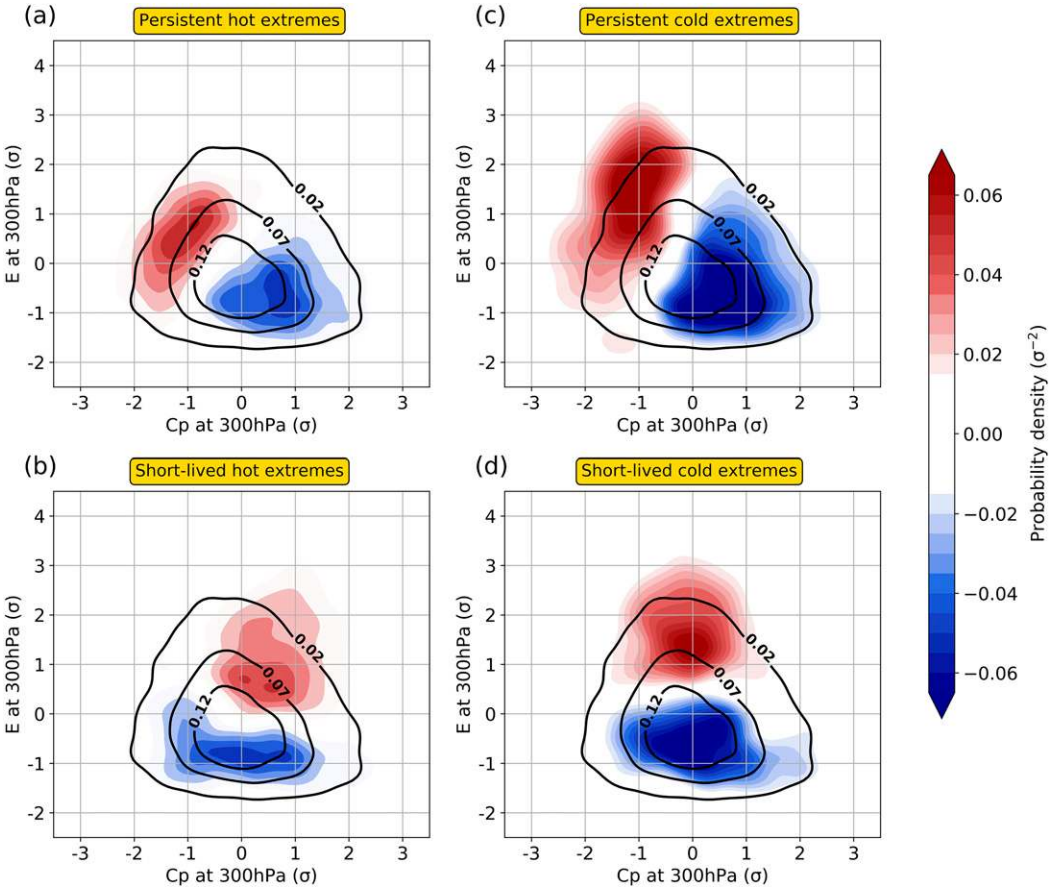

FIG. 8. Two-dimensional KDE of the normalized area-averaged daily mean E against c_p at 300 hPa. Black contours correspond to the climatology (1979–2018), while the color shading depicts the anomaly during (a) persistent and (b) short-lived hot extremes, and (c) persistent and (d) short-lived cold extremes over central Europe. The KDE bandwidth parameter for climatology is 0.21, for persistent (short-lived) hot extremes it is 0.39 (0.36) and for persistent (short-lived) cold extremes it is 0.34 (0.38).

one-dimensional Gaussian kernels, the optimal bandwidth value of which (see caption of Fig. 7) is determined using a 10-fold cross-validation (Kohavi 1995; Pedregosa et al. 2011) (see also section 10 in the SM).

For a more complete analysis of the role of RWP properties on temperature extremes, we compute the c_p–E space distribution during the four types of temperature extremes (Fig. 8). The black contours in all panels of Fig. 8 depict the climatological distribution of the normalized c_p and E time series (a discussion on its triangular shape is included in section 8 of the SM) and the color shading shows the anomaly of the distribution during the four types of temperature extremes. All distributions are derived using a two-dimensional Gaussian KDE, where a 10-fold cross-validation is again employed for the bandwidth value optimization. During persistent hot and cold extremes there is a shift of the distributions toward higher E and lower c_p with respect to climatology (Figs. 8a,c). During short-lived extremes, a similar shift toward higher E is again evident, but c_p either remains unchanged (cold extremes; Fig. 8d) or even increases (hot extremes; Fig. 8b).

The synoptic situation during the four types of temperature extremes is examined in composite means of the nonnormalized c_p, E, and Z' fields. Since these fields have a pronounced annual cycle, we focus on JJA hot extremes and DJF cold extremes for this analysis. As implied from the previous results, c_p is lower over central Europe and surrounding areas during the persistent hot and cold extremes than the short-lived ones (Fig. 9). Furthermore, in all cases, areas of enhanced RWP amplitude extend over parts of the North Atlantic and Europe, with a more pronounced signal for the DJF cases. During hot extremes, an area of increased geopotential height is located over central Europe, at a relatively short distance to the northeast of the affected

Unauthenticated | Downloaded 08/28/22 02:25 AM UTC

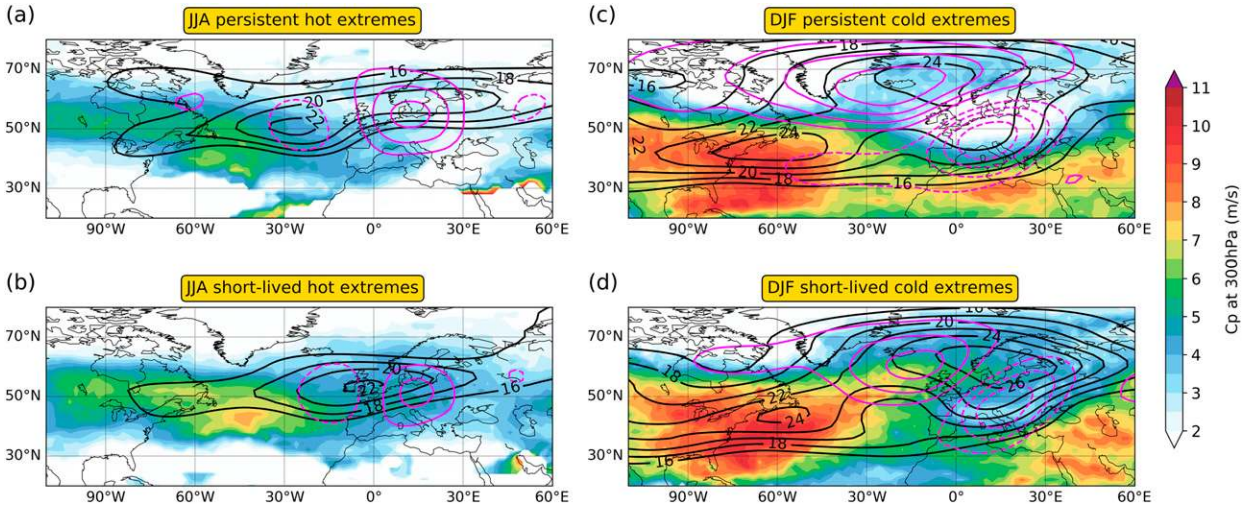

FIG. 9. Composite mean of the c_p (color shading), E (black contours at 18, 20, 22, 24 m s^{-1}), and Z' at 500 hPa (magenta contours at ±4, ±8, ±12, ±16 gpdam) daily mean fields during extreme temperature days over central Europe. (a) JJA persistent hot, (b) JJA short-lived hot, (c) DJF persistent cold, and (d) DJF short-lived cold extremes. For Z', solid (dashed) contours correspond to positive (negative) anomalies.

region. This high pressure system is more prominent in the composite of the persistent extremes and accompanied by weaker negative anomalies upstream and downstream of it. Finally, a pronounced dipole characterizes DJF persistent and—to a slightly lesser extent—short-lived cold extremes. In particular, the wide positive Z anomaly over the North Atlantic indicates the presence of a blocking anticyclone, accompanied by a strong trough at its southeastern flank (see also Pfahl 2014).

Overall, the results in this section verify—in a quantitative fashion—our expectations regarding the properties of the large-scale upper-tropospheric flow during temperature extremes in central Europe. Persistent hot and cold extremes are associated with an above-normal RWP amplitude and a below-normal RWP phase speed. The latter appears to be a distinguishing factor with short-lived temperature extremes, which are typically associated with phase speeds closer to the climatological mean value.

6. Summary and further remarks

In this study, we investigate properties of the horizontal RWP propagation and propose a method for the diagnosis of RWP phase speed and group velocity locally in space and time. Our approach involves computing the analytic signal of upper-tropospheric meridional wind along latitude circles for the detection of local RWP zonal phase speed. The zonal and meridional components of local group velocity are diagnosed by applying the same scheme to the envelope function of RWP objects. Using ERA5 reanalysis data for the time period 1979–2018, we present global climatologies of RWP amplitude and the aforementioned fields. A distinct seasonal and interregional variability is observed in the respective RWP properties, while differences and similarities between the Northern and Southern Hemispheres are apparent. Finally, we identify pronounced anomalies in the RWP amplitude and zonal phase speed distributions over central Europe during short-lived and/or persistent temperature extremes.

The main advantages of the proposed diagnostics are that they provide a local and instantaneous view on the highly dynamic evolution of RWPs and that their applicability is not limited to linear (small-amplitude) waves. Limitations of the analytic signal approach to compute the local and instantaneous phase of meridional wind and RWP amplitude are discussed in section 3. In essence, the analyzed signals (v'_ℓ, E'_ℓ, and E'_n) need to correspond, ''locally'' in space and time, to an almost plane wave of clearly discernible dominant wavenumber and angular frequency. Spatially filtering the v' and E fields, restricting the calculations to grid points where the RWP amplitude exceeds a minimum threshold (E_0), and following an object-based approach for the analytic signal computation of RWP amplitude, are the main steps in our methodology that are intended on satisfying this condition. Cases of coherent RWP propagation, as in the barotropic model example of section 3, are thus associated with a smooth evolution of the c_p and $\mathbf{c}_g$ fields. Amid the complexity of the upper-tropospheric flow, the aforementioned condition is not expected to be

Unauthenticated | Downloaded 08/28/22 02:25 AM UTC

uniformly satisfied and cases of spurious values in the c_p and $\mathbf{c}_g$ fields are to be expected. They may occur when RWPs undergo merging and splitting (as determined by the E_0 threshold) and the almost plane wave form of the v'_ℓ, E'_ℓ, and E'_n signals is distorted, or when they reach a highly nonlinear stage and break.[5] The local variations in the c_p and $\mathbf{c}_g$ fields of such cases should be interpreted with caution.

The presented analyses have been tested for their sensitivity to variations in the parameter values. The climatological analyses of sections 4 and 5 are not sensitive to slight variations in the filtering of v' and E fields. In addition, changes in the precise value of the minimum length and width thresholds ($\mathscr{L}_0$ and $\mathscr{N}_0$) in the group velocity diagnosis (section 3c), do not lead to a noticeable change on the results. Although there is no substantial change in the spatial patterns of Figs. 4 and 5 with an increase of the E_0 threshold to $20\,\mathrm{m\,s^{-1}}$, the c_p and c_{gx} magnitudes at regions of zonal wind maxima are decreased by about 0.25 and $1\,\mathrm{m\,s^{-1}}$, respectively, while the magnitude of c_{gy} increases by about $0.25\,\mathrm{m\,s^{-1}}$. In this case the sample at each grid point consists of higher-amplitude RWPs, the propagation of which in a more decelerated zonal flow is less confined in the zonal direction. A decrease of the threshold to $10\,\mathrm{m\,s^{-1}}$ leads to the opposite changes (see also section 6 in the SM). Furthermore, it should be noted that the presented climatological patterns are expected to slightly vary in magnitude and position for different isobaric levels than the 300 hPa used here. The 300-hPa level is a good compromise since it captures the annual cycle of the main upper-tropospheric circulation features of the two hemispheres and allows the comparison of our analyses with past studies. Nevertheless, the respective climatologies of Figs. 4 and 5 at the level of 200 hPa are included in section 5 of the SM for reference, together with a brief discussion on qualitative and quantitative differences. Finally, the analyses shown in Figs. 7 and 8 do not change qualitatively for the individual seasons and for variations on the aforementioned parameters.

The analyses in section 5 constitute a climatological assessment of the role of large-scale upper-tropospheric flow properties during central European temperature extremes. Investigating the mechanisms that lead to RWPs of large amplitude and low phase speed and the multiscale interactions that determine the eventual magnitude of temperature anomalies in Europe are beyond the scope of this paper. Fragkoulidis et al. (2018) provide further evidence on the role of RWP amplitude and its temporal evolution through a statistical analysis of European temperature extremes and an investigation of the 2003 and 2010 heat waves in Europe and Russia, respectively. Furthermore, the study of Zschenderlein et al. (2018) explores the interplay between RWP properties and smaller-scale physical processes in the case of the late-summer 2016 heat wave in Europe. Future analyses in this regard will hopefully benefit from the availability of the presented RWP diagnostics.

Overall, the proposed diagnostics capture effectively and with low computational demands local features of the RWP spatiotemporal evolution. They can thus facilitate, among other things, a better understanding of the RWP's interplay with smaller-scale processes, an objective partition into propagating and stationary waves, and thorough investigations into the role of the large-scale upper-tropospheric flow in weather extremes. Finally, future studies may further utilize these diagnostics for the investigation of processes that can alter the properties of the large-scale circulation at weather and climate time scales, without obscuring features that exhibit zonal asymmetries.

Acknowledgments. The research leading to these results has been done within the Transregional Collaborative Research Center SFB/TRR 165 "Waves to Weather" (www.wavestoweather.de) funded by the German Research Foundation (DFG). We are grateful to three anonymous reviewers for their insightful and constructive remarks, as well as to Paolo Ghinassi for providing the barotropic model data, and the Copernicus Climate Change Service for providing access to the reanalysis data. We would also like to thank Lukas Papritz for insightful discussions regarding the Southern Hemisphere climatologies. Finally, we gratefully acknowledge the computing time granted on the supercomputer Mogon at the Johannes Gutenberg University Mainz (hpc.uni-mainz.de).

REFERENCES

Ahmadi-Givi, F., M. Nasr-Esfahany, and A. R. Mohebalhojeh, 2014: Interaction of North Atlantic baroclinic wave packets and the Mediterranean storm track. *Quart. J. Roy. Meteor. Soc.*, **140**, 754–765, https://doi.org/10.1002/qj.2171.

Baumgart, M., P. Ghinassi, V. Wirth, T. Selz, G. C. Craig, and M. Riemer, 2019: Quantitative view on the processes governing the upscale error growth up to the planetary scale using a stochastic convection scheme. *Mon. Wea. Rev.*, **147**, 1713–1731, https://doi.org/10.1175/MWR-D-18-0292.1.

Berbery, E. H., and C. S. Vera, 1996: Characteristics of the Southern Hemisphere winter storm track with filtered and unfiltered data. *J. Atmos. Sci.*, **53**, 468–481, https://doi.org/10.1175/1520-0469(1996)053<0468:COTSHW>2.0.CO;2.

Blackmon, M. L., Y.-H. Lee, J. M. Wallace, and H.-H. Hsu, 1984: Time variation of 500 mb height fluctuations with long, intermediate

[5] Enhanced overturning in such cases will imply a weakening in the magnitude of the meridional wind and its envelope (see also Ghinassi et al. 2018).

Unauthenticated | Downloaded 08/28/22 02:25 AM UTC

and short time scales as deduced from lag-correlation statistics. *J. Atmos. Sci.*, **41**, 981–991, https://doi.org/10.1175/1520-0469(1984)041<0981:TVOMHF>2.0.CO;2.

Branstator, G., 2002: Circumglobal teleconnections, the jet stream waveguide, and the North Atlantic Oscillation. *J. Climate*, **15**, 1893–1910, https://doi.org/10.1175/1520-0442(2002)015<1893:CTTJSW>2.0.CO;2.

Cai, M., and B. Huang, 2013: A dissection of energetics of the geostrophic flow: Reconciliation of Rossby wave energy flux and group velocity. *J. Atmos. Sci.*, **70**, 2179–2196, https://doi.org/10.1175/JAS-D-12-0249.1.

Chang, E. K. M., 1993: Downstream development of baroclinic waves as inferred from regression analysis. *J. Atmos. Sci.*, **50**, 2038–2053, https://doi.org/10.1175/1520-0469(1993)050<2038:DDOBWA>2.0.CO;2.

——, 1999: Characteristics of wave packets in the upper troposphere. Part II: Seasonal and hemispheric variations. *J. Atmos. Sci.*, **56**, 1729–1747, https://doi.org/10.1175/1520-0469(1999)056<1729:COWPIT>2.0.CO;2.

——, 2001a: GCM and observational diagnoses of the seasonal and interannual variations of the Pacific storm track during the cool season. *J. Atmos. Sci.*, **58**, 1784–1800, https://doi.org/10.1175/1520-0469(2001)058<1784:GAODOT>2.0.CO;2.

——, 2001b: The structure of baroclinic wave packets. *J. Atmos. Sci.*, **58**, 1694–1713, https://doi.org/10.1175/1520-0469(2001)058<1694:TSOBWP>2.0.CO;2.

——, 2005: The impact of wave packets propagating across Asia on Pacific cyclone development. *Mon. Wea. Rev.*, **133**, 1998–2015, https://doi.org/10.1175/MWR2953.1.

——, and I. Orlanski, 1994: On energy flux and group velocity of waves in baroclinic flows. *J. Atmos. Sci.*, **51**, 3823–3828, https://doi.org/10.1175/1520-0469(1994)051<3823:OEFAGV>2.0.CO;2.

——, and D. B. Yu, 1999: Characteristics of wave packets in the upper troposphere. Part I: Northern Hemisphere winter. *J. Atmos. Sci.*, **56**, 1708–1728, https://doi.org/10.1175/1520-0469(1999)056<1708:COWPIT>2.0.CO;2.

——, S. Lee, and K. L. Swanson, 2002: Storm track dynamics. *J. Climate*, **15**, 2163–2183, https://doi.org/10.1175/1520-0442(2002)015<02163:STD>2.0.CO;2.

Chaudhury, K. N., and M. Unser, 2009: Construction of Hilbert transform pairs of wavelet bases and Gabor-like transforms. *IEEE Trans. Signal Process.*, **57**, 3411–3425, https://doi.org/10.1109/TSP.2009.2020767, 0908.3380.

Cohen, L., 1995: *Time-Frequency Analysis*. Prentice Hall, 299 pp.

Copernicus Climate Change Service (C3S), 2017: ERA5: Fifth generation of ECMWF atmospheric reanalyses of the global climate. Copernicus Climate Change Service Climate Data Store (CDS), accessed February 2019, https://cds.climate.copernicus.eu/cdsapp#!/home.

Coumou, D., V. Petoukhov, S. Rahmstorf, S. Petri, and H. J. Schellnhuber, 2014: Quasi-resonant circulation regimes and hemispheric synchronization of extreme weather in boreal summer. *Proc. Natl. Acad. Sci. USA*, **111**, 12 331–12 336, https://doi.org/10.1073/pnas.1412797111.

Dickinson, R. E., 1978: Rossby waves–long-period oscillations of oceans and atmospheres. *Annu. Rev. Fluid Mech.*, **10**, 159–195, https://doi.org/10.1146/annurev.fl.10.010178.001111.

Domeisen, D. I. V., O. Martius, and B. Jiménez-Esteve, 2018: Rossby wave propagation into the Northern Hemisphere stratosphere: The role of zonal phase speed. *Geophys. Res. Lett.*, **45**, 2064–2071, https://doi.org/10.1002/2017GL076886.

Esler, J. G., 2004: Benjamin–Feir instability of Rossby waves on a jet. *Quart. J. Roy. Meteor. Soc.*, **130**, 1611–1630, https://doi.org/10.1256/qj.03.74.

——, and P. H. Haynes, 1999a: Baroclinic wave breaking and the internal variability of the tropospheric circulation. *J. Atmos. Sci.*, **56**, 4014–4031, https://doi.org/10.1175/1520-0469(1999)056<4014:BWBATI>2.0.CO;2.

——, and ——, 1999b: Mechanisms for wave packet formation and maintenance in a quasigeostrophic two-layer model. *J. Atmos. Sci.*, **56**, 2457–2490, https://doi.org/10.1175/1520-0469(0)056<2457:MFWPFA>2.0.CO;2.

Feldstein, S. B., and U. Dayan, 2008: Circumglobal teleconnections and wave packets associated with Israeli winter precipitation. *Quart. J. Roy. Meteor. Soc.*, **134**, 455–467, https://doi.org/10.1002/qj.225.

Fragkoulidis, G., V. Wirth, P. Bossmann, and A. H. Fink, 2018: Linking Northern Hemisphere temperature extremes to Rossby wave packets. *Quart. J. Roy. Meteor. Soc.*, **144**, 553–566, https://doi.org/10.1002/qj.3228.

Gabor, D., 1946: Theory of communication. Part I: The analysis of information. *J. Inst. Electr. Eng.*, **93**, 429–441, https://doi.org/10.1049/JI-3-2.1946.0074.

Gabriel, A., and D. Peters, 2008: A diagnostic study of different types of Rossby wave breaking events in the northern extratropics. *J. Meteor. Soc. Japan*, **86**, 613–631, https://doi.org/10.2151/jmsj.86.613.

Ghinassi, P., G. Fragkoulidis, and V. Wirth, 2018: Local finite-amplitude wave activity as a diagnostic for Rossby wave packets. *Mon. Wea. Rev.*, **146**, 4099–4114, https://doi.org/10.1175/MWR-D-18-0068.1.

Glatt, I., and V. Wirth, 2014: Identifying Rossby wave trains and quantifying their properties. *Quart. J. Roy. Meteor. Soc.*, **140**, 384–396, https://doi.org/10.1002/qj.2139.

——, A. Dörnbrack, S. Jones, J. Keller, O. Martius, A. Müller, D. H. Peters, and V. Wirth, 2011: Utility of Hovmöller diagrams to diagnose Rossby wave trains. *Tellus*, **63A**, 991–1006, https://doi.org/10.1111/j.1600-0870.2011.00541.x.

Grazzini, F., and F. Vitart, 2015: Atmospheric predictability and Rossby wave packets. *Quart. J. Roy. Meteor. Soc.*, **141**, 2793–2802, https://doi.org/10.1002/qj.2564.

Hakim, G. J., 2003: Developing wave packets in the North Pacific storm track. *Mon. Wea. Rev.*, **131**, 2824–2837, https://doi.org/10.1175/1520-0493(2003)131<2824:DWPITN>2.0.CO;2.

Harris, F. J., 1978: On the use of windows for harmonic analysis with the discrete Fourier transform. *Proc. Inst. Electr. Electron. Eng.*, **66**, 51–83, https://doi.org/10.1109/PROC.1978.10837.

Haurwitz, B., 1940: The motion of atmospheric disturbances on the spherical earth. *J. Mar. Res.*, **3**, 254–267.

Hayashi, Y., 1982: Space-time spectral analysis and its applications to atmospheric waves. *J. Meteor. Soc. Japan*, **60**, 156–171, https://doi.org/10.2151/jmsj1965.60.1_156.

Held, I. M., and B. J. Hoskins, 1985: Large-scale eddies and the general circulation of the troposphere. *Advances in Geophysics*, Vol. 28, Academic Press, 3–31, https://doi.org/10.1016/S0065-2687(08)60218-6.

Hoskins, B. J., and T. Ambrizzi, 1993: Rossby wave propagation on a realistic longitudinally varying flow. *J. Atmos. Sci.*, **50**, 1661–1671, https://doi.org/10.1175/1520-0469(1993)050<1661:RWPOAR>2.0.CO;2.

Hovmöller, E., 1949: The trough-and-ridge diagram. *Tellus*, **1**, 62–66, https://doi.org/10.3402/tellusa.v1i2.8498.

Hsu, H.-H., 1987: Propagation of low-level circulation features in the vicinity of mountain ranges. *Mon. Wea. Rev.*, **115**, 1864–1893, https://doi.org/10.1175/1520-0493(1987)115<1864:POLLCF>2.0.CO;2.

Unauthenticated | Downloaded 08/28/22 02:25 AM UTC

Huang, N. E., and Coauthors, 1998: The empirical mode decomposition and the Hilbert spectrum for nonlinear and non-stationary time series analysis. *Proc. Roy. Soc. London*, **A454**, 903–995, https://doi.org/10.1098/rspa.1998.0193.

——, Z. Wu, S. R. Long, K. C. Arnold, X. Chen, and K. Blank, 2009: On instantaneous frequency. *Adv. Adapt. Data Anal.*, **1**, 177–229, https://doi.org/10.1142/S1793536909000096.

Inatsu, M., and B. J. Hoskins, 2004: The zonal asymmetry of the Southern Hemisphere winter storm track. *J. Climate*, **17**, 4882–4892, https://doi.org/10.1175/JCLI-3232.1.

Joung, C. H., and M. H. Hitchman, 1982: On the role of successive downstream development in East Asian polar air outbreaks. *Mon. Wea. Rev.*, **110**, 1224–1237, https://doi.org/10.1175/1520-0493(1982)110<1224:OTROSD>2.0.CO;2.

Kohavi, R., 1995: A study of cross-validation and bootstrap for accuracy estimation and model selection. *Proc. 14th Int. Joint Conf. on Artificial Intelligence*, Montreal, QC, Canada, IJCAI, 1137–1143.

Lee, S., and I. M. Held, 1993: Baroclinic wave packets in models and observations. *J. Atmos. Sci.*, **50**, 1413–1428, https://doi.org/10.1175/1520-0469(1993)050<1413:BWPIMA>2.0.CO;2.

Marple, L. S., 1999: Computing the discrete-time "analytic" signal via FFT. *IEEE Trans. Signal Process.*, **47**, 2600–2603, https://doi.org/10.1109/78.782222.

Martius, O., C. Schwierz, and H. C. Davies, 2010: Tropopause-level waveguides. *J. Atmos. Sci.*, **67**, 866–879, https://doi.org/10.1175/2009JAS2995.1.

Nakamura, H., 1992: Midwinter suppression of baroclinic wave activity in the Pacific. *J. Atmos. Sci.*, **49**, 1629–1642, https://doi.org/10.1175/1520-0469(1992)049<1629:MSOBWA>2.0.CO;2.

——, and J. M. Wallace, 1990: Observed changes in baroclinic wave activity during the life cycles of low-frequency circulation anomalies. *J. Atmos. Sci.*, **47**, 1100–1116, https://doi.org/10.1175/1520-0469(1990)047<1100:OCIBWA>2.0.CO;2.

——, and A. Shimpo, 2004: Seasonal variations in the Southern Hemisphere storm tracks and jet streams as revealed in a reanalysis dataset. *J. Climate*, **17**, 1828–1844, https://doi.org/10.1175/1520-0442(2004)017<1828:SVITSH>2.0.CO;2.

O'Brien, L., and M. J. Reeder, 2017: Southern Hemisphere summertime Rossby waves and weather in the Australian region. *Quart. J. Roy. Meteor. Soc.*, **143**, 2374–2388, https://doi.org/10.1002/qj.3090.

Orlanski, I., and E. K. M. Chang, 1993: Ageostrophic geopotential fluxes in downstream and upstream development of baroclinic waves. *J. Atmos. Sci.*, **50**, 212–225, https://doi.org/10.1175/1520-0469(1993)050<0212:AGFIDA>2.0.CO;2.

Papritz, L., S. Pfahl, H. Sodemann, and H. Wernli, 2015: A climatology of cold air outbreaks and their impact on air-sea heat fluxes in the high-latitude South Pacific. *J. Climate*, **28**, 342–364, https://doi.org/10.1175/JCLI-D-14-00482.1.

Pedlosky, J., 2003: *Waves in the Ocean and Atmosphere: Introduction to Wave Dynamics*. Springer Berlin Heidelberg, 264 pp., https://doi.org/10.1007/978-3-662-05131-3.

Pedregosa, F., R. Weiss, and M. Brucher, 2011: Scikitlearn: Machine learning in Python. *J. Mach. Learn. Res.*, **12**, 2825–2830, https://doi.org/10.1007/s13398-014-0173-7.2, 1201.0490.

Pfahl, S., 2014: Characterising the relationship between weather extremes in Europe and synoptic circulation features. *Nat. Hazards Earth Syst. Sci.*, **14**, 1461–1475, https://doi.org/10.5194/nhess-14-1461-2014.

Pierrehumbert, R. T., and K. L. Swanson, 1995: Baroclinic instability. *Annu. Rev. Fluid Mech.*, **27**, 419–467, https://doi.org/10.1146/annurev.fl.27.010195.002223.

Plumb, R. A., 1986: Three-dimensional propagation of transient quasi-geostrophic eddies and its relationship with the eddy forcing of the time–mean flow. *J. Atmos. Sci.*, **43**, 1657–1678, https://doi.org/10.1175/1520-0469(1986)043<1657:TDPOTQ>2.0.CO;2.

Quinting, J. F., and F. Vitart, 2019: Representation of synoptic-scale Rossby wave packets and blocking in the S2S prediction project database. *Geophys. Res. Lett.*, **46**, 1070–1078, https://doi.org/10.1029/2018GL081381.

Randel, W. J., and I. M. Held, 1991: Phase speed spectra of transient eddy fluxes and critical layer absorption. *J. Atmos. Sci.*, **48**, 688–697, https://doi.org/10.1175/1520-0469(1991)048<0688:PSSOTE>2.0.CO;2.

Rhines, P., 2015: Dynamical meterology—Rossby waves. *Encyclopedia of Atmospheric Sciences*, 2nd ed. G. R. North, J. Pyle, and F. Zhang, Eds., Academic Press, 404–416, https://doi.org/10.1016/B978-0-12-382225-3.00346-7.

Rossby, C. G., 1940: Planetary flow patterns in the atmosphere. *Quart. J. Roy. Meteor. Soc.*, **66**, 68–97.

Röthlisberger, M., O. Martius, and H. Wernli, 2018: Northern Hemisphere Rossby wave initiation events on the extratropical jet—A climatological analysis. *J. Climate*, **31**, 743–760, https://doi.org/10.1175/JCLI-D-17-0346.1.

——, L. Frossard, L. F. Bosart, D. Keyser, and O. Martius, 2019: Recurrent synoptic-scale Rossby wave patterns and their effect on the persistence of cold and hot spells. *J. Climate*, **32**, 3207–3226, https://doi.org/10.1175/JCLI-D-18-0664.1.

Ruxton, G. D., 2006: The unequal variance *t*-test is an underused alternative to Student's *t*-test and the Mann-Whitney U test. *Behav. Ecol.*, **17**, 688–690, https://doi.org/10.1093/beheco/ark016.

Schemm, S., and T. Schneider, 2018: Eddy lifetime, number, and diffusivity and the suppression of eddy kinetic energy in midwinter. *J. Climate*, **31**, 5649–5665, https://doi.org/10.1175/JCLI-D-17-0644.1.

Schoon, L., and C. Zülicke, 2018: A novel method for the extraction of local gravity wave parameters from gridded three-dimensional data: Description, validation, and application. *Atmos. Chem. Phys.*, **18**, 6971–6983, https://doi.org/10.5194/acp-18-6971-2018.

Simmons, A. J., and B. J. Hoskins, 1979: The downstream and upstream development of unstable baroclinic waves. *J. Atmos. Sci.*, **36**, 1239–1254, https://doi.org/10.1175/1520-0469(1979)036<1239:TDAUDO>2.0.CO;2.

Souders, M. B., B. A. Colle, and E. K. M. Chang, 2014a: A description and evaluation of an automated approach for feature-based tracking of Rossby wave packets. *Mon. Wea. Rev.*, **142**, 3505–3527, https://doi.org/10.1175/MWR-D-13-00317.1.

——, ——, and ——, 2014b: The climatology and characteristics of Rossby wave packets using a feature-based tracking technique. *Mon. Wea. Rev.*, **142**, 3528–3548, https://doi.org/10.1175/MWR-D-13-00371.1.

Takaya, K., and H. Nakamura, 2001: A formulation of a phase-independent wave-activity flux for stationary and migratory quasigeostrophic eddies on a zonally varying basic flow. *J. Atmos. Sci.*, **58**, 608–627, https://doi.org/10.1175/1520-0469(2001)058<0608:AFOAPI>2.0.CO;2.

Teubler, F., and M. Riemer, 2016: Dynamics of Rossby wave packets in a quantitative potential vorticity–potential temperature framework. *J. Atmos. Sci.*, **73**, 1063–1081, https://doi.org/10.1175/JAS-D-15-0162.1.

Thorncroft, C. D., B. J. Hoskins, and M. E. McIntyre, 1993: Two paradigms of baroclinic-wave life-cycle behaviour. *Quart. J. Roy. Meteor. Soc.*, **119**, 17–55, https://doi.org/10.1002/qj.49711950903.

Unauthenticated | Downloaded 08/28/22 02:25 AM UTC

Vallis, G. K., 2017: *Atmospheric and Oceanic Fluid Dynamics: Fundamentals and Large-Scale Circulation*. 2nd ed. Cambridge University Press, 946 pp., https://doi.org/10.1017/9781107588417.

Vanneste, J., and T. G. Shepherd, 1998: On the group-velocity property for wave-activity conservation laws. *J. Atmos. Sci.*, **55**, 1063–1068, https://doi.org/10.1175/1520-0469(1998)055<1063:OTGVPF>2.0.CO;2.

Wernli, H., and M. Sprenger, 2007: Identification and ERA-15 climatology of potential vorticity streamers and cutoffs near the extratropical tropopause. *J. Atmos. Sci.*, **64**, 1569–1586, https://doi.org/10.1175/JAS3912.1.

White, R. H., D. S. Battisti, and G. H. Roe, 2017: Mongolian mountains matter most: Impacts of the latitude and height of Asian orography on Pacific wintertime atmospheric circulation. *J. Climate*, **30**, 4065–4082, https://doi.org/10.1175/JCLI-D-16-0401.1.

Wirth, V., and J. Eichhorn, 2014: Long-lived Rossby wave trains as precursors to strong winter cyclones over Europe. *Quart. J. Roy. Meteor. Soc.*, **140**, 729–737, https://doi.org/10.1002/qj.2191.

——, M. Riemer, E. K. M. Chang, and O. Martius, 2018: Rossby wave packets on the midlatitude waveguide—A review. *Mon. Wea. Rev.*, **146**, 1965–2001, https://doi.org/10.1175/MWR-D-16-0483.1.

Wolf, G., and V. Wirth, 2015: Implications of the semigeostrophic nature of Rossby waves for Rossby wave packet detection. *Mon. Wea. Rev.*, **143**, 26–38, https://doi.org/10.1175/MWR-D-14-00120.1.

——, and ——, 2017: Diagnosing the horizontal propagation of Rossby wave packets along the midlatitude waveguide. *Mon. Wea. Rev.*, **145**, 3247–3264, https://doi.org/10.1175/MWR-D-16-0355.1.

Zimin, A. V., I. Szunyogh, D. J. Patil, B. R. Hunt, and E. Ott, 2003: Extracting envelopes of Rossby wave packets. *Mon. Wea. Rev.*, **131**, 1011–1017, https://doi.org/10.1175/1520-0493(2003)131<1011:EEORWP>2.0.CO;2.

Zschenderlein, P., G. Fragkoulidis, A. H. Fink, and V. Wirth, 2018: Large-scale Rossby wave and synoptic-scale dynamic analyses of the unusually late 2016 heatwave over Europe. *Weather*, **73**, 275–283, https://doi.org/10.1002/wea.3278.

Unauthenticated | Downloaded 08/28/22 02:25 AM UTC